LOW DIMENSIONAL STRUCTURES FOR OPTICAL AND ELECTRICAL APPLICATIONS

A THESIS
SUBMITTED TO THE DEPARTMENT OF PHYSICS
AND THE INSTITUTE OF ENGINEERING AND SCIENCE
OF BILKENT UNIVERSITY
IN PARTIAL FULFILLMENT OF THE REQUIREMENTS
FOR THE DEGREE OF
MASTER OF SCIENCE

By
İmran Akça
July, 2008

I certify that I have read this thesis and that in my opinion it is fully adequate, in scope and in quality, as a thesis for the degree of Master of Science.

Prof. Dr. Atilla Aydınlı(Advisor)

I certify that I have read this thesis and that in my opinion it is fully adequate, in scope and in quality, as a thesis for the degree of Master of Science.

Prof. Dr. Şefik Süzer

I certify that I have read this thesis and that in my opinion it is fully adequate, in scope and in quality, as a thesis for the degree of Master of Science.

Assist. Prof. Dr. Ceyhun Bulutay

Approved for the Institute of Engineering and Science:

Prof. Dr. Mehmet B. Baray
Director of the Institute

ABSTRACT

LOW DIMENSIONAL STRUCTURES FOR OPTICAL AND ELECTRICAL APPLICATIONS

İmran Akça
M.S. in Physics
Supervisor: Prof. Dr. Atilla Aydınlı
July, 2008

Low dimensional structures such as quantum dots have been particularly attractive because of their fundamental physical properties and their potential applications in various devices in integrated optics and microelectronics. This thesis presents optical and electrical applications of low dimensional structures. For this purpose we have studied silicon and germanium nanocrystals for flash memory applications and InAs quantum dots for optical modulators.

As a quantum dot, nanocrystals can be used as storage media for carriers in flash memories. Performance of a nanocrystal memory device can be expressed in terms of write/erase speed, carrier retention time and cycling durability. Charge and discharge dynamics of PECVD grown nanocrystals were studied. Electron and hole charge and discharge currents were observed to differ significantly and strongly depend on annealing conditions chosen for the formation of nanocrystals. Our experimental results revealed that, discharge currents were dominated by the interface layer acting as a quantum well for holes and route for direct tunneling for electrons.

On the other hand, possibility of obtaining quantum dots with enhanced electro-optic and/or electro-absorption coefficients makes them attractive for use in light modulation. Therefore, waveguides of multilayer InAs quantum dots were studied. Electro-optic measurements were conducted at 1.5 μm and clear Fabry-Perot resonances were obtained. The voltage dependent Fabry-Perot measurements revealed that 6 V was sufficient for full on/off modulation. Electro-absorption measurements were conducted at both 1.3 and 1.5 μm. Since the structure lases at 1285 nm, high absorption values at 1309 nm were obtained. The absorption spectrum of the samples was also studied under applied electric field. Absorption spectra of all samples shift to lower photon energies with

increasing electric field.

Keywords: Silicon nanocrystals, Germanium nanocrystals, nonvolatile memories, quantum dots, electro-optic modulation, electro-absorption modulation, optical waveguides.

ÖZET

DÜŞÜK BOYUTLU YAPILARIN ELEKTİRİK VE OPTİK UYGULAMALARI

İmran Akça
Fizik Bölümü, Yüksek Lisans
Tez Yöneticisi: Prof. Dr. Atilla Aydınlı
Temmuz, 2008

Kuvantum nokta gibi düşük boyutlu yapılar, sahip oldukları fiziksel özellikleri, optik ve mikro-elektronikteki geniş uygulama alanları ile oldukça ilgi çekmektedir. Bu tezde düşük boyutlu yapıların optik ve elektrikteki uygulamalarindan bahsedilmektedir. Bu amaçla silikon ve germanyum nanokristal içeren kalıcı hafızalara ve InAs kuvantum nokta içeren optik kipleyicilere yönelik çalışmalar yapılmıştır.

Aslında birer kuvantum nokta olan nanokristaller yük depolayabildikleri için kalıcı hafıza olarak da kullanılabilmeleri olasıdır. Nanokristal belleklerin performansı yazma/silme hızı, yük tutma süresı ve devir süresi ile belirlenmektedir. PECVD metodu ile üretilen nanokristalerin şarj ve deşarj özellikleri incelenmiştir. Elektron ve deşiklerin şarj, deşarj akımlarının pişirme sıcaklıklarına bağlı olarak birbirinden farklılık gösterdiği gözlemlenmiştir. Deney sonuçlarına göre, deşiklerin deşarj akımının kuvantum kuyusu gibi davranan ara yüz tabakası tarafından, elektronların deşarj akımının ise direk tünelleme tarafından sağlandığı gözlemlenmiştir.

Diğer taraftan, kuvantum noktaların yüksek elektro-optik ve elektro-soğurma katsayılarına sahip olma olasılıkları, bu malzemeleri ışığın modülasyonu açısından oldukça önemli kılmaktadır. Bu amaçla, InAs kuvantum noktalar içeren dalga kılavuzu yapıları uzerinde calışılmıştır. Elektro-optik ölçümleri 1.5 μm dalga boyunda gerçekleştirilmiş ve Fabry-Perot rezonansları elde edilmiştir. Fabry-Perot ölçümlerinin sonuçlarına göre, 6 V için ışık tamamen açılıp kapatılabilmektedir. Elektro-soğurma ölçümleri 1.3 ve 1.5 μm dalga boylarında gerçekleştirilmiştir. Kullanılan yapılar gerçekte lazer olarak tasarlanmış ve 1285 nm'de ışıyan yapılar oldukları için en yüksek soğurma değerleri 1309 nm'de

elde edilmiştir. Soğurma eğrileri uygulanan gerilim altında incelenmiş ve artan gerilimle beraber soğurma eğrilerinin düsük foton enerjilerine doğru kaydıkları gözlemlenmiştir.

Anahtar sözcükler: Silikon nanokristal, Germanyum nanokristal, kalıcı hafıza, kuvantum nokta, elektro-optik modülasyon, elektro-soğurma modülasyon, optik dalga kılavuzları .

Acknowledgement

First and foremost, I would like to thank my research advisor, Professor Atilla Aydınlı. I knew Professor Aydınlı since I was a first year senior student. He offered me an excellent opportunity, when I asked about working in his laboratory during the summer. I have been happily working for Professor Aydınlı ever since. I admire his personality and broad knowledge very much. He helped me generously and gave me tremendous support over the years. I have benefited a lot from his continuous encouragement and invaluable advice. I am also very impressed by his enthusiasm for the scientific pursuit. I feel very fortunate for the opportunity to have him as my research advisor.

I am very thankful to Assistant Professor Aykutlu Dana. I learned a lot from him in both experimental and theoretical analysis of the nanocrystal nonvolatile memories. He has been supportive of my work and I also enjoyed taking his excellent courses.

I am indebted to the former members of the Integrated Optics Group, Feridun Ay, İsa Kiyat, and Selcen Aytekin for helping me get through the initial learning stage as a new integrated optics group student.

I am also thankful to the current members of the Integrated Optics Group, Aşkın Kocabaş, Ayşe Erbil, Seçkin Şenlik, and Samet Yumrukçu for their friendship and support.

I am also particularly grateful to Selim Olçum for his friendship and numerous technical discussions.

I would like to thank Professor Raşit Turan at Middle East Technical University, Turkey, Professor Nadir Dağlı at University of California, Santa Barbara, USA for the discussions and collaboration. I am also grateful to Professor Andrea Fiore at Ecole Polytechnique Federale de Lausanne (EPFL), Switzerland for InAs quantum dot samples, and Assistant Professor Aykutlu Dana for germanium nanocrystal samples.

I would also like to thank our laboratory physicist, Murat Güre and technician Ergün Karaman for their technical support during my research.

I would like to acknowledge Umut Bostancı, for collaborations on silicon nanocrystal optical waveguide project. I am very grateful to him for his support in clean room processes.

I am also grateful to the numerous help from other clean room folks. Among them were Münir Dede, Rohat Melik, and Tuncay Özel.

I am also appreciative of the financial support I received through a fellowship from TÜBİTAK.

I would like to thank to all staff of the Institute of Materials Science and Nanotechnology for their invaluable support during my research.

I am also thankful to the directors of the UNAM, Professor Salim Çıracı and Assistant Professor Mehmet Bayındır for providing excellent facilities in UNAM.

I would like to thank my family and Akın Avcı for their love, support and encouragement.

Finally, I want to thank and acknowledge my thesis examination committee: Professors Atilla Aydınlı, Ceyhun Bulutay, and Şefik Süzer.

Contents

1 Introduction **1**

1.1 Fundamentals of Nanoparticles 1

1.1.1 Silicon and Germanium Nanocrystals 2

1.1.2 Quantum Dots 5

1.2 Thesis Outline 7

2 Silicon and Germanium Nanocrystal MOS Capacitors for Memory Applications **9**

2.1 Introduction 9

2.2 Experimental 12

2.2.1 Preparation of Germanium Nanocrystals 12

2.2.2 Preparation of Silicon Nanocrystals 13

2.2.3 Fabrication of Nanocrystal MOS Capacitors 21

3 Modelling of Nanocrystal MOS Capacitors **24**

3.1 Fundametals of MOS Capacitors 24

3.2 Basic Conduction Mechanisms for MOS Capacitors 27
3.3 Fundamentals of Nanocrystal MOS capacitor 29
3.3.1 Charging of Nanocrystal MOS capacitors 29
3.3.2 Discharging of Nanocrystal MOS Capacitors 30

4 Electrical Characterization of Nanocrystal MOS Capacitors 34
4.1 Germanium Nanocrystal MOS Capacitors 34
4.1.1 High Frequency Capacitance-Voltage Measurements 34
4.1.2 Flat-band Voltage Measurements 35
4.1.3 Charging of Nanocrystals 36
4.1.4 Discharging of Nanocrystals 37
4.2 Silicon Nanocrystal MOS Capacitors 39
4.2.1 Flat-Band Measurements 39
4.2.2 Charging of Nanocrystals 42
4.2.3 Discharging of Nanocrystals 42
4.3 Conclusions 43

5 Electro-optic and Electro-absorption Properties of InAs Quantum Dot Waveguides 45
5.1 Introduction 45
5.2 InAs Quantum Dot Waveguides Under Applied Field 50
5.2.1 InAs QD Waveguide Structures 50

5.2.2 Measurement Set-up 51
5.3 Simulations of InAs Quantum Dot Waveguides 52
5.4 Measurements and Results 55
5.4.1 Electro-optical Measurements 55
5.4.2 Electro-absorption Measurements 58
5.5 Conclusions 60

6 Conclusions **62**

List of Figures

2.1 Plama enhanced chemical vapor deposition mechanism. 12

2.2 Formation of Ge NCs as a function of anneal temperature and GeH_4 flow rate as observed by TEM. Multi-layer structures of germanosilicate with flow rates of 120, 110, 100 and 90 sccm are seen away from the substrate (bottom to top) after annealing at a) 650 ^oC, b) 770 ^oC, and c) 850 ^oC for 5 minutes. 14

2.3 Experimental set-up of the photoluminescence 15

2.4 Effect of Si concentration on the photoluminescence. Si rich silicon nitride films with varying NH_3 flow rates were investigated. Note that the redshift in photoluminesce curve with increasing Si concentration. 16

2.5 Effect of annealing temperature and time on the photoluminescence. Annealed and unannealed Si rich silicon dioxide films were used for this experiment. The PL curve is maximum for 1200 ^oC and 1 hour annealing conditions. 18

2.6 Set-up for ellipsometry measurements. 19

2.7 Ellipsometric study of Si-rich SiO_2 films with varying annealing temperatures and times. 20

2.8 Refractive index values of Si-rich silicon nitride film between 500 and 1000 nm. 21

2.9 Nanocrystal MOS fabrication fabrication steps. 22

2.10 **(a)** A glass barrier is placed over a part of the silicon substrate for shielding the plasma. Under this barrier no material growth is observed. **(b)** This figure illustrates the structure of the sample after PECVD gradient growth method. 23

3.1 A MOS capacitor structure with Si-ncs are used as floating gate. . 25

3.2 **a)**During accumulation, electrons detrapped from nanocrystals with the applied positive gate voltage.**b)** 26

3.3 During inversion electrons trapped inside the nanocrystals by applying negative positive voltage to the gate electrode. 27

3.4 Schematic representation of the Fowler Nordheim tunneling under high voltage. In here Φ_B barrier height, E_{FM} metal Fermi level, E_{FS} semiconductor Fermi level, d_{ox} oxide thickness, d_{FN} tunneling distance, and V_{gate} gate voltage 28

4.1 Experimental data of charging of n (right) and p (left) type capacitors. Charging currents as a function of charge voltage are measured for samples annealed at 700-800 ^oC. 36

4.2 Discharge current densities as a function of time for n and p type devices (in terms of substrate types). The holes decay faster than the electrons for samples annealed at low temperatures whereas they decay much slower for samples annealed at higher temperatures. 37

4.3 Band structure of Ge nanocrystal MOS capacitor, a) annealed at low temperatures, b) annealed at high temperatures. Note the effect of quantum well at the interface and the increased nanocrystal size. 39

4.4 Cumulative flat-band voltage shift as a function of pulse voltage. Tunnel oxide layer was grown by gradient growth method. The dip beyond 15 V indicates the in-layer charge motion. 40

4.5 For this sample gradient growth method was applied to the nanocrystal formation layer. At 15 V of pulse voltage in-layer charge motion is seen which corresponds to a negative hysteresis. . 41

4.6 Cumulative flat-band voltage shift of the sample which was not grown by gradient growth method. Charge motion is observed inside the nanocrytstal layer and at the oxide-nitride interface at specific voltages. 41

4.7 Cumulative flat-band voltage shift of the stoichiometric sample as a function of the pulse voltage. Note that there is no in-layer charge motion for this sample. 42

4.8 Decay of the stored charges of the Si-nc MOS capacitors which has a gradually increasing layers. With increasing thickness decay rate of the charges decreases. 43

5.1 EL data and detailed structure of the InAs quantum dot waveguides. 51

5.2 Measurement set-up for electrical and optical measurements. . . . 52

5.3 Fundamental mode profile of the InAs quantum dot waveguides for TE polarization. The effective index of the structure is obtained as 3.27 from simulation. 54

5.4 Fundamental mode profile of the InAs quantum dot waveguides for TM polarization. The effective index of the structure is obtained as 3.248 from simulation 54

5.5 Fabry-Perot resonances at 1515 nm for 6 Volt reverse bias. The dots show the experimental data and the line indicates the optimum curve fit. 56

5.6 Voltage dependent shift of Fabry-Perot resonances. Significant tuning is observed with relatively low voltages. 56

5.7 Variation in refractive index as a function of applied voltage at 1515 nm. The dots show the experimental data and the line indicates the linear fit. 57

5.8 The graphical representation of the calculation of overlap factor. The confinement factor is calculated from this overlap region by simply integrating the shaded area. 59

5.9 Change in absorption due to applied reverse bias for 1 mm long sample. Red shift of the spectra should be noted with increasing applied voltage. 60

5.10 Change in absorption due to applied reverse bias for 1.6 mm long sample. 60

Chapter 1

Introduction

1.1 Fundamentals of Nanoparticles

Nanoparticles are zero-dimensional structures with a diameter varying between one to few hundreds of nanometers. When the dimensions of the material are scaled down to nanometer range, the atomic and electronic structures may gain some unique features which make the material favorable for many applications. The properties of the nanoparticles are mostly size dependent. For small nanoparticles, the properties vary and they are specific to each size. At large sizes, nanoparticles would have the properties similar to bulk.

The main mechanism that triggers the unusual behavior of the nanoparticles is quantum confinement. Quantum confinement model is based on the effective-mass approximation theory. It is an inherent concept for all the low-dimensional structures, such as quantum wells, quantum wires, and quantum dots, which display confinement in 1, 2 and 3 dimensions, respectively.

Quantum confinement becomes effective when the particles dimensions are comparable to exciton Bohr radius. According to the quantum confinement theory, electrons in the conduction band and holes in the valence band are confined spatially by the potential barrier. Bound states are formed in the quantum wells

energies of which are determined by the potential of the barrier and the well width as well as other material parameters. The case of the quantum dots represent the ultimate confinement configuration with discrete energy states due to confinement in all directions. The density of states also changes dramatically from the bulk case, reducing along the direction of confinement and ultimately reaching atom like discrete states. It is well known from basic quantum mechanics that as the width of the spatial confinement decreases energy separation between the bound states increases. Therefore, the energy that is required for the optical transition from valence band to conduction band increases and as a result, effective band gap increases relative to the bulk value [31].

Thus, quantum confinement model can also explain the blue shift of the luminescence spectrum with decreasing of the particle size. According to the model, the emission wavelength and intensity depend on the nanoparticle diameter, size distribution, and concentration.

Nanoparticles can be amorphous or crystalline and when they are crystalline they are called as nanocrystals. In this thesis, we will mainly concentrate on silicon nanocrystals (Si-nc) and germanium nanocrystals (Ge-nc).

1.1.1 Silicon and Germanium Nanocrystals

Silicon is the material of choice in the microelectronic industry. This remarkable success is due to various factors such as the wide availability of silicon and its good thermal and mechanical properties that make it easy to manufacture silicon based devices. On the other hand, silicon has an indirect band-gap structure that limits the optical emission and hence modulation.

Porous silicon was the first material that has been reported to display an intense photoluminescence [8]. After that, Si-ncs have become popular for their relatively high quality of luminescence efficiency properties. The luminescence of Si nanocrystals has been studied in single layer and multi layer structures and relatively high efficient electroluminescence (EL) values were obtained [9].

Si-ncs and Ge-ncs may have a radii close to or smaller than the exciton Bohr radius. Once the diameter becomes smaller than the exciton radius, the energy levels in the particle become quantized and the transitions are locked into specific energy states. The term silicon nanocrystal refers to a range of materials around the transition region from amorphous to microcrystalline phase in the silicon thin film. It is similar to amorphous silicon (a-Si) but it has many useful advantages over the a-Si in the extreme limit of small size. First, if grown properly it can have a higher electron mobility. Second, it shows increased absorption in the red and infrared wavelengths, which makes it an important material for use in solar cells. Third, it has lower hydrogen concentration.

Ge-ncs have smaller band gap compared to silicon. Therefore, Ge-ncs are thought to be better suited for data retention operations than Si-ncs in non volatile memory applications.

There is a impressive number of papers in the literature reporting that photonic excitation of Si-ncs and Ge-ncs induces a strong luminescence [15, 38]. Typically, the luminescence spectrum covers the visible and the near-infra red regions, from 600 nm to 1000 nm. The physical mechanisms associated with luminescence is still controversial. Different models have been proposed to explain both the intense luminescence and the higher photon energy. The quantum confinement model is widely used to explain experimental results. Due to the quantum confinement effect, the luminescence spectrum of the nanocrystals shifts to lower photon energies (blue shift) with decrease of the nanocrystal size, and enhanced emission is observed.

According to quantum confinement model, the energy that is required for the emission of a photon, depends on the nanocrystal size. Brus et.al proposed an analytical model to relate the quantum confinement effect and confinement radius in nanocrystals. When the higher order terms are neglected, the relationship between the energy and size is given as [5]:

$$E_{g,NC} = E_{g,bulk} - \frac{1.8q_e^2}{\epsilon R} + \frac{\hbar^2\pi^2}{2\mu R^2} + O\left(\frac{1}{R^3}\right) \tag{1.1}$$

where $E_{g,NC}$ is the lowest eigenvalue for the confined exciton, $E_{g,bulk}$ is the bulk material bandgap, μ is the reduced mass of the electron-hole pair, and R is the radius of the nanocrystal . The factor 1.8 that appears in Coulomb attraction term accounts for the overlap of electron and hole wave functions.

Several different techniques have been used to produce Si-nc and Ge-ncs such as: plasma enhanced chemical vapour deposition (PECVD) [20], sputtering deposition [47], pulsed laser deposition (PLD) [48], physical vapour deposition (PVD) [52], ion implantation [13], all followed by thermal annealing. Extensive studies have been carried out to better understand the basic mechanisms of nanocrystal production and growth. Experimental PL and EL emission from these nanocrystals typically depend on both the nanocrystal size as well as the size distribution of these nanocrystals.

Si and Ge nanocrystal based devices become popular after the realization of unique properties of the nanocrystals. Si-nc and Ge-nc based photoluminescent displays, light emitting diodes (LED), optical waveguides and non-volatile memories have been extensively studied.

Meldrum et al. have been active in the area of Si-nc array photoluminescent displays. They have fabricated Fabry-Perot microcavity resonators by growing a silicon rich oxide (SRO) layer between two silver films of 200 nm and 20 nm, followed by annealing at 500 ^{o}C. A HeCd laser emitting at 325 nm was used for the PL excitation. By varying the SRO layer thickness, they tuned the light emission in the range from 475 nm to 875 nm, covering most of the visible region. The emitted light was bright enough to be recordable by means of a digital camera [32].

Enhanced light emission of the Si-ncs triggered the research on Si-nc based light emitting diodes and a huge number of article has been published on this topic [14, 21]. The first reported result on the fabrication of Si-nc based LEDs was obtained with porous n-doped silicon. A thin (12 nm) gold layer was used for the contact. In 1996, Hirschman et al. published possibly the first attempt to integrate a Si-nc (PS) LED with microelectronic circuit [14]. In their work, they used a bipolar transistor to modulate light emission in controlling the current

flow through the LED. The most efficient Si-nc based LED has been obtained by Cho and co-workers who reported an external quantum efficiency of 1.6% [21]. The Si-nc were produced in a silicon nitride layer by PECVD and was sandwiched between n-type SiC and p-type Si.

In an effort to further improve the current status of the flash memories many approaches are under study including the use of nanocrystals. Nanocrystal based non volatile memories is therefore a popular topic among the others. The charge, discharge and retention dynamics of the Si-ncs memories are being studied and the obtained results are promising. In the first part of this thesis, we study the electrical properties of semiconducting nanocrystal based MOS capacitors in order to understand their charge and dischage characteristics. This work is a good example of an electrical application of low dimensional structures in the form of nanocrystals.

1.1.2 Quantum Dots

One of the major problems involved in nanocrystal research is the inhomogeneity of the particles which causes inhomogeneous broadening effects in the PL and EL spectrum. This problem can be minimized by preparing uniform nanoparticles in the form of quantum wells, wires, or dots.

Quantum dot is a zero dimensional structure which is spatially confined in three dimensions and is characterized by a completely discrete energy spectrum. Such structures can be produced by modern epitaxial growth techniques. The epitaxial growth techniques have a very slow growth rate, which allow one to control very accurately the dimension in the growth directions. The well known epitaxial growth techniques of molecular beam epitaxy (MBE) and metal organic chemical vapor deposition (MOCVD) achieve monolayer control in the growth direction.

The Stranski-Krastanov growth mechanism is used to explain formation of self-assembled quantum dots in MBE and MOCVD systems. In this method,

the lattice mismatch between substrate and the deposited material results in strain in the crystal lattice. As more material is deposited, it eventually becomes energetically more favorable for the material to form islands. As a result, three-dimensional islands are formed rather than a uniform film. Density and size of these quantum dots can be controlled using computer controlled growth conditions.

This thesis is concerned specifically with the InAs/InGaAs combination. The lattice constant of InAs is approximately 7% greater than the lattice constant of InGaAs. When InAs is deposited on InGaAs layer, significant strain develops at the interface. Beyond a critical thickness of InAs, the growth mode changes from layer-by-layer growth to the formation of three-dimensional islands. When the InAs islands are capped with a second layer of InGaAs, the islands form three dimensional potential wells, known as self assembled quantum dots. These quantum dots typically have base sizes of 10 nm, but much less is known about their physical size, shape and composition.

Quantum dots are particularly significant for optical applications due to their theoretically high quantum yield. They are specifically intented for use in quantum computing, laser, light emitting diodes, and photovoltaic devices. The quantum dot lasers will be discussed in this section.

Semiconductor lasers are key components in optical communications. The basis of laser operation depends on the creation of nonequilibrium populations of electrons and holes. In 1970, C. Henry proposed that, using quantum wells as the active layers in a laser would result in more efficient devices operating at lower threshold currents than lasers with bulk active layers. In addition, the use of a quantum well, provides the tuning capability of the wavelength. In 1975, the first quantum well laser was demonstrated, but it was many times less efficient than a conventional laser. After the realization of new materials growth capabilities (MBE), more efficient structures have been fabricated.

Quantum dots were the promising materials for lasers. Arakawa and Sakaki predicted that quantum dot lasers should exhibit less temperature dependent performance than existing semiconductor lasers [4]. Other benefits of quantum

dot active layers include further reduction in threshold currents and an increase in differential gain. Thus, quantum dot lasers with high quality, uniform quantum dots in the active layer have become popular.

Fiore et al. have worked on InAs/GaAs quantum dot lasers and obtained high gain values for these structures [16]. They built InAs quantum dot based quantum dot laser lasing at 1280 nm using a ridge waveguide structure. The quantum dots were sandwiched between a p-type and an n-type layer to form a p-n junction. Quantum dot lasers were studied under forward bias. However, little is known on the reverse biased characteristics of these structures. In the second part of this thesis, we report the electro-optical properties of these InAs quantum dots for possible use in optical modulators.

1.2 Thesis Outline

This thesis presents optical and electrical applications of low dimensional structures. The chapters are organized as follows:

In Chapter 2, we discuss the design, fabrication, and characterization of silicon and germanium nanocrystal layers made by plasma enhanced chemical vapor deposition. Photoluminescence, raman scattering, transmission electron microscopy, and ellipsometry measurements are used for characterization of nanocrystals. Moreover, the effects of the nanocrystal size, density and annealing temperature and time on the photoluminescence are studied. Finally, the fabrication of Si-nc and Ge-nc MOS capacitors are presented.

In Chapter 3, the modelling of the charging and discharging mechanism of silicon and germanium nanocrystal MOS capacitors are studied. These devices are silicon and germanium nanocrystal floating gate MOS capacitors designed to correlate the optical properties of silicon and germanium nanocrystals to the charging and discharging mechanisms. We use the model that we proposed earlier, which assumes charge storage in quantized energy levels of nanocrystal instead of deep traps.

In Chapter 4, charge and discharge measurements of nanocrystal MOS capacitors are explained and results are given. Electron and hole charge and discharge dynamics are studied. Electron and hole charge and discharge currents are observed to differ significantly and depend strongly on annealing conditions chosen for the formation of nanocrystals. At low annealing temperatures, holes are seen to charge slower but to escape faster than electrons. They discharge slower than electrons when annealing temperatures are raised. We demonstrate that discharge currents are dominated by the interface layer acting as a quantum well for holes and by direct tunneling for electrons.

Chapter 5 describes the electro-absorption and electro-optical properties of InAs quantum dot waveguide structures under an applied electric field. After giving the definition of electro-optic and electro-absorption effects, the test devices are described in detail. The electrical and optical characterization of the structures are explained and the measurement set-up is given. For electro-optic measurements, the Fabry-Perot Interferometer method is used and the voltage dependent Fabry-Perot resonances are obtained. The experimental results are fitted to well known Fabry-Perot transmission formula and electro-optic coefficient for InAs quantum dots is obtained. The results reveal that enhanced electro-optic coefficient is obtained for InAs quantum dot based ridge optical waveguides compared to bulk GaAs. For electro-absorption measurements, optical transmission experiments are conducted under varying voltages. The results indicate that with increasing voltage change in absorption increases and absorption edge shifts to lower photon energies. The electro-optical and the electro-absorption demonstrates that InAs quantum dots are good candidates for modulator applications.

In Chapter 6, a brief summary of the performed studies and the conclusions reached are given and future directions for research in these topics are suggested.

Chapter 2

Silicon and Germanium Nanocrystal MOS Capacitors for Memory Applications

2.1 Introduction

Recently, nonvolatile memory devices utilizing nanocrystals in floating gate devices have received considerable attention due to their promising memory performance and high scalability. In nanocrystal memory devices, nanocrystals such as semiconductors [39], metals [23], and compound semiconductors [51] are sandwiched between the control oxide and the tunneling oxide layers as charge storage nodes to replace the continuous floating gate layer which are used in conventional memories.

The nonvolatile Si-nc and Ge-nc memories have been extensively studied. A complete review of the literature exceeds the scope of this thesis, so we will briefly review some general features reported in the literature focusing especially on charge and discharge dynamics of carriers in nanocrystal memories.

Busseret et al. have studied nonvolatile memory devices, which were basically MOS capacitors. The polysilicon floating gate was replaced by LPCVD grown Si-ncs where nanocrystals acts as storage node. They showed that the approach of De Salvo on charge and discharge dynamics of the nanocrystals is not completely appropriate for experimental observations. They proposed a so-called granular model in which electrons interact with the nanocrystals one by one. The experimental results indicated that charge dynamics of Si-ncs were related to the number of Si-ncs occupied by one charge and not to the average number of charges per Si-nc [6].

Campera and Iannaccone have studied the charging and discharging processes in Si-nc flash memories during write/erase operations. As a result of the experimental studies and numerical simulations, they have shown that electrons are stored in quantum confined states in the nanocrystal conduction band. They have also focused on the effect of hydrogen annealing on the role of traps in the nanocrystals during charging and discharging mechanisms [7].

Yang et al. have observed the charge trapping and retention in Ge-ncs. For this purpose, a MOS structure with Ge-ncs distributed in the gate oxide was fabricated. Ge-ncs were synthesized using the low-energy Ge ion implantation which was followed by a thermal annealing at 800 ^oC. They have observed that, electron trapping had occurred at both negative and positive charging voltages, on the other hand holes were trapped at only positive charging voltages. The retention time of the electrons are long in the case of positive charging [29].

She et al. have studied the write/erase speed of Ge-nc memory devices. By using single-charge tunneling theory, they have proposed a model to describe the retention. The effects of nanocrystal size, tunnel-oxide thickness, and high-k tunnel material on the device performance were studied. They have shown that Ge-nc memory devices could provide at least 10^6 times larger retention-time to write-time ratio than conventional floating-gate devices. They have proposed that the device performance could be enhanced using high-k, and low barrier tunel materials [44].

Koh et al. have worked on effects of traps on charge and discharge mechanisms of Ge-nc memories. Transistor and capacitor structures with Ge-ncs were fabricated to study the trap energy levels. Temperature dependent measurements were conducted to observe the effect of the traps on Ge-nc charging dynamics. Nanocrystal size and the trap energy-level relationship for a long-term charge retention performance was extracted from simulation results [22].

Sousa et al. have presented electron- and hole-based data storage operations in Si_{1-x}-Ge_x nanocrystal nonvolatile memories. Due to the lower confinement barrier, electrons are removed much faster than holes which makes holes more appropriate for long charge retention operations. The only disadvantage of the hole-based operation was slower data programming in comparison to electrons. Additionally, they have observed that that the increase of Ge composition reduces the electron retention time [12].

Kanoun et al. have investigated the charging effects in Ge-ncs embedded in SiO_2 matrix fabricated by LPCVD technique. They have used capacitance-voltage (CV) and currentvoltage (IV) analysis. In C-V measurements, a hysteresis was observed which indicates that holes are charging in the Ge islands. Different ramp times were used in C-V measurements to demonstrate the hole charging is the origin of the transient current. I-V measurements have demonstrated the charging effects and hysteresis was observed only at low temperatures [28].

Despite all of the above, charge and discharge characteristics of nanocrystal and where the charges are stored are not well known. We, therefore, in this thesis study the charge and discharge characteristics of nanocrystals and explore the possibility of charge storage in the quantized levels of the nanocrystals. Effects of high temperature annealing on the performance of the nanocrystal based MOS capacitors are also presented.

2.2 Experimental

2.2.1 Preparation of Germanium Nanocrystals

PECVD Deposition

Plasma-enhanced chemical vapor deposition (PECVD) is a technique commonly used in micro-fabrication to deposit layers of insulating materials and amorphous or polycrystalline silicon. The plasma is used to help stimulate a reaction on the substrate surface of two or more spices from the gas phase. The major advantage of PECVD is, its lower temperature capability with respect to other systems, such as conventional CVD. For example, for silicon deposition in a CVD system , the required temperature is 700-900 ^oC, on the other hand, this value decreases to 250-350 ^oC in a PECVD system. The schematic representation of a PECVD system is given in Figure 2.1.

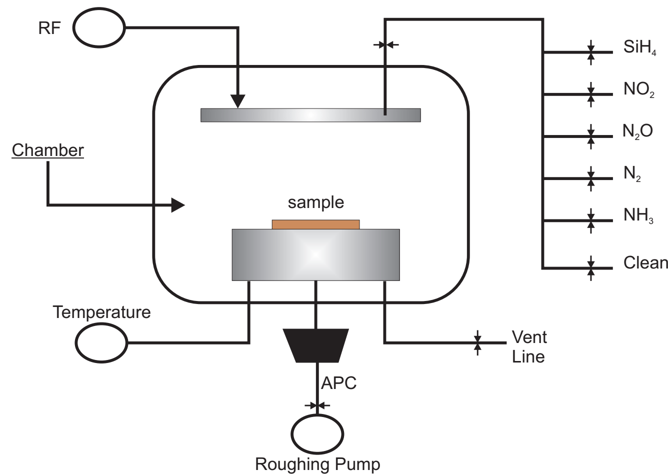

Figure 2.1: Plama enhanced chemical vapor deposition mechanism.

The germanosilicate films were grown using a parallel-plate type PECVD reactor (Plasmalab 8510C). 180 sccm SiH_4 (2% in N_2), 225 sccm NO_2 and varying flow rates of GeH_4 (2% in He) were used. The sample temperature and process pressure were 350 ^oC, 1000 mTorr, respectively. 10 W of RF power was applied during the deposition. After deposition, germaniumsilicate films were annealed at high temperature in order to provide phase seperation between oxide and

germanium.

Annealing

In Ge-nc formation processes, typical temperatures for nanocrystal formation vary between 600-800 ^oC. Therefore, the PECVD grown germanosilicate films were annealed at temperatures ranging from 650 to 850 ^oC for duration of 5 minutes under nitrogen environment. Since Ge diffuses into SiO_2 very fast, even at relatively low temperatures Ge-ncs are easily formed by diffusion. At high temperatures and low annealing times it may also diffuse to the interface. Presence of Ge at the interface creates an interface layer, which has to be considered in the analysis of flash memories.

Characterization

The PECVD grown germanosilicate films were characterized using transmission electron microscopy (TEM).

Transmission electron microscopy (TEM) images of a multilayered Ge-nc sample show the formation of nanocrystals as a function of annealing temperature as seen in Figure 2.2. The layers contain increasing amounts of Ge in layers away from the silicon substrate. The nanocrystals are clearly seen as black spots on the image, with their nearly spherical shape and uniform size. Using TEM data, the size of the nanocrystals were estimated. The nanocrystal diameter increases nonlinearly from 2.5 nm to 7.4 nm as the annealing temperature is increased from 650 ^oC to 850 ^oC.

TEM data provide us the information on processing parameters to obtain Ge nanocsrytals.

2.2.2 Preparation of Silicon Nanocrystals

PECVD Deposition

In PECVD, SiH_4 and NO_2 gases are used for the deposition of silicon dioxide

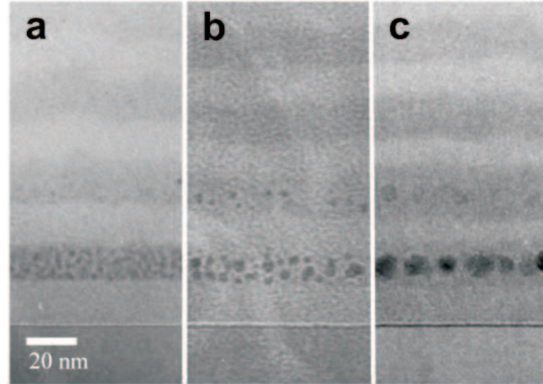

Figure 2.2: Formation of Ge NCs as a function of anneal temperature and GeH_4 flow rate as observed by TEM. Multi-layer structures of germanosilicate with flow rates of 120, 110, 100 and 90 sccm are seen away from the substrate (bottom to top) after annealing at a) 650 ^oC, b) 770 ^oC, and c) 850 ^oC for 5 minutes.

thin films. For silicon nitride thin film deposition, $SiH_4$and NH_3 gases are used. Stoichiometry of the film can be controlled by the relative flow rates of the two gases used during deposition. Excess Si content in the oxide and nitride thin films is adjusted by controlling of the flow rates of the source gases (SiH_4, N_2O, and NH_3).

We deposited Si-rich silicon dioxide or Si-rich silicon nitride films by using PECVD method (Plasmalab 8510C). Si-rich silicon dioxide films were grown using 200 sccm SiH_4 (2% in N_2), 8 sccm NO_2, at a sample temperature of 250 ^oC, a process pressure of 1000 mTorr under and an applied RF power of 10 W. For Si-rich silicon nitride films the flow rate of 350 sccm for SiH_4, and 10 sccm for NH_3 were used. All other fabrication conditions were same. After the deposition, the SiO_x film was annealed at high temperature, causing the phase separation between Si and SiO_2 with the formation of Si-ncs.

Annealing

The high temperature annealing was done using alumina ovens with the ambient gas of N_2. The annealing temperatures ranging from 1100-1200 ^oC and annealing durations varying between 1 to 2 hours were studied. Although silicon nitride films were not annealed at high temperatures, Si-nc formation was

observed possibly due to high stress content of the PECVD grown nitride films. The density and size distribution of Si-ncs can be controlled by silicon content (with SiH_4 flow rate) and annealing temperature (for SiO_2 films). The change in the Si-nc size can be observed in photoluminescence (PL) measurements, if the PL peak shifts to lower photon energies, this means Si-nc size gets larger and vice versa.

Characterization

For characterization of silicon nanocrystals, photoluminescence (PL) and ellipsometry methods were used.

There are many process parameters that effect the luminescence spectrum of the PECVD grown Si-ncs. These effects can be listed as nanocrystal size and distribution, annealing temperature, time, and atmosphere. By using the PL set-up, given in the Figure 2.3, we have investigated these effects on Si-rich silicon oxide and nitride films.

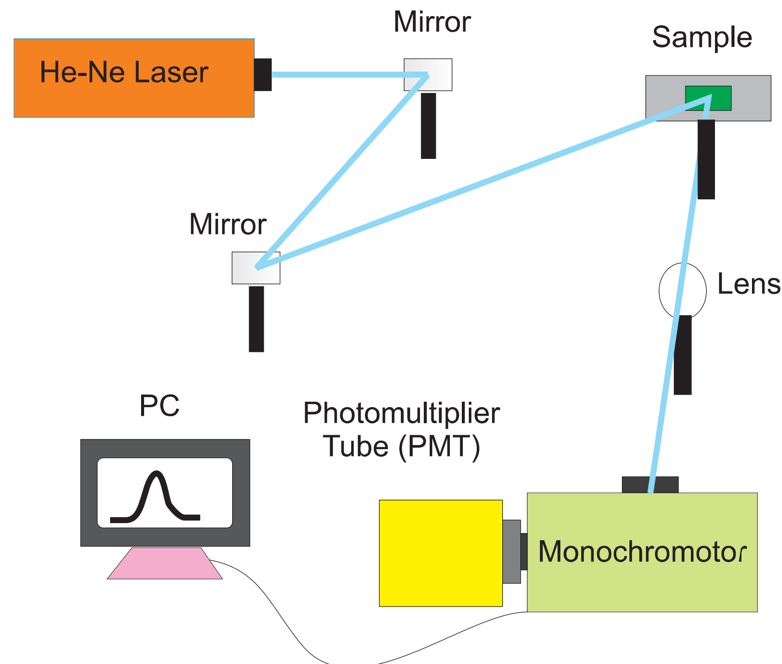

Figure 2.3: Experimental set-up of the photoluminescence

The experimental setup that is used to take PL data uses the 632 nm line of a He-Ne laser or 514.5 nm or 488 nm of an Ar+ laser as the excitation source. The

sample is illuminated using a cylindrical lens for a line focus to minimize sample heating. Photoexcited luminescence is collected by a collection lens corrected for spherical aberrations and F number matched to a double monochromator. A GaAs based photomultiplier was used in the photon counting mode to record the data.

The luminescence intensity depends on the amount of excess Si concentration. Luminescence intensity is maximum for a concentration of Si in excess equal to 30% of the SiO_2 concentration. When a larger concentration of Si is added, the luminescence signal decreases with the Si concentration. The position of the luminescence peak also red shifts with increasing Si concentration as can be seen from Figure 2.4.

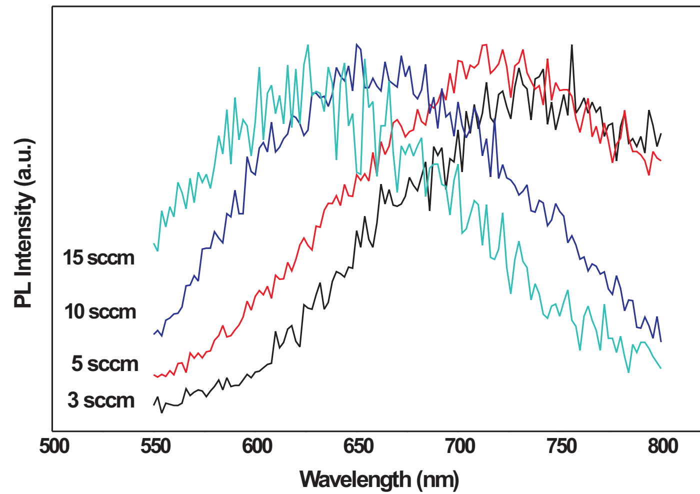

Figure 2.4: Effect of Si concentration on the photoluminescence. Si rich silicon nitride films with varying NH_3 flow rates were investigated. Note that the redshift in photoluminesce curve with increasing Si concentration.

The size of the Si-ncs were controlled by the flow rate of the NH_3 gas. Instead of varying the flow rate of SiH_4, we used a fixed SiH_4 value of 350 sccm and changed the flow rate of NH_3 between 3 to 15 sccm. An increase in NH_3 flow rate can be considered as similar to a decrease in SiH_4 flow rate. For 3 sccm of NH_3, the position of the PL peak was at about 750 nm, and this value decreased to 600 nm when the concentration of the gas reached to 15 sccm. This means the size of the Si-ncs get smaller as the NH_3 flow rates increase.

These observations can be understood within the quantum confinement model of nanocrystals since increasing Si concentrations (indicated by decreasing NH_3 flow rates) lead to formation of larger nanocrystals. Energy separation between the bound states decreases as the nanocrystal size increases leading to red shift of the observed luminescence. For us, this is a signature for the presence of Si nanocrystals allowing us to optimize the growth conditions of the layers to be used in the MOS capacitor structures

On the other hand, the Si-nc formation mechanism in SiO_2 matrix layer requires a thermal activation temperature greater than 900 ^oC which is stated by Li et al [26]. This feature suggests a growth mechanism which promotes the clustering of small Si-nc into larger Si-nc under high temperature annealing. This process is called Ostwald ripening, which is a spontaneous process that occurs because larger crystals are more energetically favored than smaller crystals. This mechanism proposes that the smaller sized Si clusters act as a source for the bigger sized clusters. As a result, disappearance of small Si clusters leads to the formation of larger sized Si nanocrystals.

Moreover annealing at high temperature can eliminate most of the defects that are formed during growth mechanism. The luminescence intensity grows as the annealing time increases and also large Si-ncs can be formed by increasing the annealing time. The annealing temperature and time were scanned for Si-ncs in silicon dioxide matrix. The results are given in Figure 2.5.

The Si-rich silicon dioxide films in Figure 2.5 were prepared using 200 sccm of SiH_4 and 8 sccm of N_2O at 350 ^oC. The minimum PL signal was obtained from as grown films as expected. For 1200 ^oC the PL peak shifted toward the lower photon energies which is a direct result of clustering of small Si-ncs into larger Si-ncs. The annealing time slightly changed the PL spectrum. For the samples that were annealed at 1100 ^oC, 2 hours of annealing resulted in a redshift in the PL which supports the formation of large Si-ncs by increased annealing time. The optimum temperature and time were obtained as 1200 ^oC and 1 hour, respectively for Si-rich silicon dioxide films.

The choice of annealing environment (N_2, Ar, air, H_2) can drastically affect

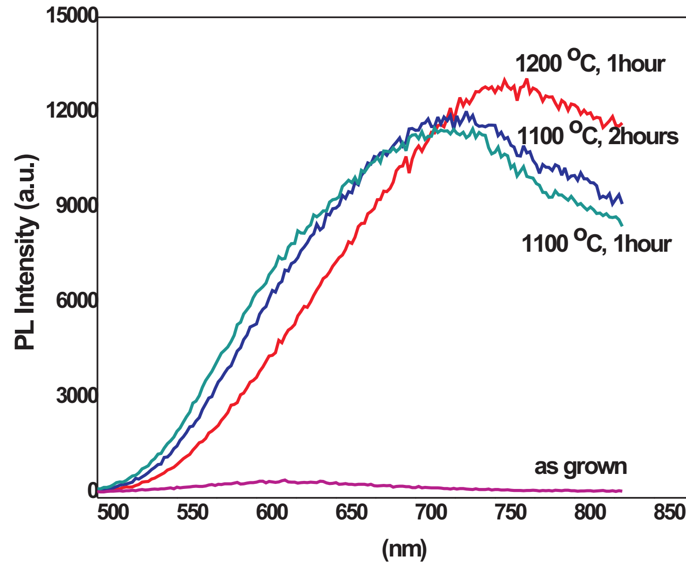

Figure 2.5: Effect of annealing temperature and time on the photoluminescence. Annealed and unannealed Si rich silicon dioxide films were used for this experiment. The PL curve is maximum for 1200 ^oC and 1 hour annealing conditions.

the shape and the intensity of the luminescence emission spectra [50]. The ambient gas during annealing can be used for passivation of the samples. In hydrogen environment, luminescence can increase by as much as one order of magnitude (11). This increase in luminescence is attributed to the termination of dangling bonds by hydrogen atoms which are responsible for non-radiative recombination. Passivation can also induce a blueshift or a redshift of the PL spectrum. This data is indicative of the presence of Si nanocrystals and their size which is important in the design and fabrication of Si nanocrystal based MOS capacitors.

Optical ellipsometry was used to determine the optical properties (refractive index and extinction coefficient) of Si-ncs layers in the wavelength range from 400 to 1000 nm. The experimental set-up is given in Figure 2.6.

The ellipsometer is a commercial device made by Wollam Inc. It is a variable angle spectroscopic device capable of taking data in a wide range of incidence angles as well as wavelengths.

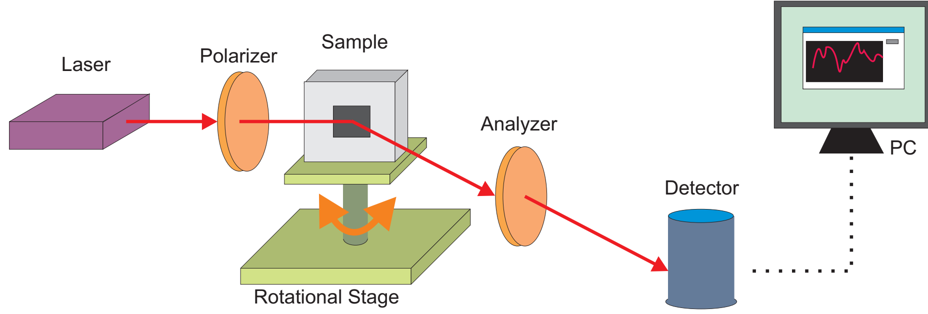

Figure 2.6: Set-up for ellipsometry measurements.

Tauc-Lorentz dispersion model was used to describe the Si-ncs optical properties. It is based on the determination of the imaginary part, ϵ_2 , of the dielectric function. The energy dependence of ϵ_2 is modeled as the product of the Tauc joint density of states with a Lorentz oscillator [3]:

$$\epsilon_2(E) = \begin{cases} \frac{1}{E}\frac{AE_0C(E-E_g)^2}{\left(E^2-E_0^2\right)+C^2E^2} & for E > E_g \\ 0 & otherwise \end{cases} \tag{2.1}$$

In this formula, only one oscillator is used. The parameters A, C, E_0 represent the amplitude and broadening of the oscillator and the peak transition energy, respectively. E_g is the optical band gap. The real part of the dielectric function ϵ_1 is obtained by Kramers Kronig integration of ϵ_2.

For ellipsometric measurements, two sets of samples were prepared, one with Si-rich silicon nitride and one with Si-rich silicon dioxide films. The optimum sample thickness was determined as 250 nm to obtain a reasonably high PL intensity and to avoid interference effects in ellipsometric measurements. The effect of PECVD gas flow rates and annealing temperatures on optical properties were studied by scanning each parameter.

Before ellipsometric studies, PL measurements were conducted, and the sample that did not show any luminescence effect, was not considered for ellipsometric measurements so that, the number of parameters were limited. The Si-rich silicon dioxide films in Figure 2.6 were prepared using 200 sccm of SiH_4 and 8 sccm of NO_2 at 350 ^oC. After ellipsometric measurements, the refractive index as high

as 2.0 in the UV was obtained for Si-rich nitride films, and 1.8 for annealed Si-rich oxide films. For comparison, the refractive index of what is considered as the stoichiometric silicon dioxide and silicon nitride films were also measured and refractive index values of 1.45 for silicon dioxide and 1.7 for silicon nitride films were obtained at 800 nm. The change in refractive index of Si-rich oxide films with annealing temperature and time is given in Figure 2.7.

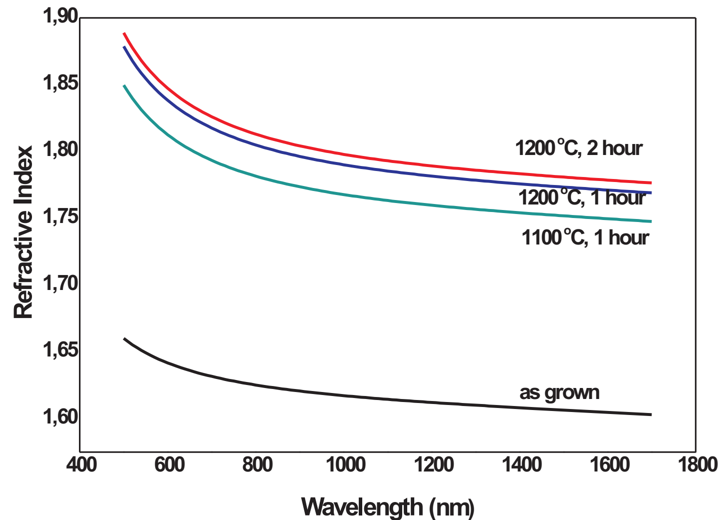

Figure 2.7: Ellipsometric study of Si-rich SiO_2 films with varying annealing temperatures and times.

The refractive index of the unannealed sample was obtained as 1.62 at 800 nm. This value increased with the increasing annealing temperature and reached to 1.81 for annealing at 1200 ^oC for 2 hours. High temperature annealing triggers the phase separation between Si and SiO_2 and resulted in larger nanocrystal formation. What was earlier a mixed matrix of SiO_2 laced with Si atoms is now SiO_2 with clusters of Si nanocrystals. The sample that was annealed at 1200 ^oC for 2 hours had the highest refractive index value of 1.81. The effect of annealing time become insignificant beyond a critical value, which may be considered as the saturation of the phase separation between Si and SiO_2. Again, the results of ellipsometric studies are indicative of the formation of Si nanocrystals and allows us to determine the growth conditions for the formation of Si nanocrystals.

The optical properties of Si-rich silicon nitride films prepared by using 350

sccm of SiH_4 and varying flow rates of NH_3 between 5 to 10 sccm were studied using ellipsometry, and the refractive index change as a function of the wavelength is given in Figure 2.8

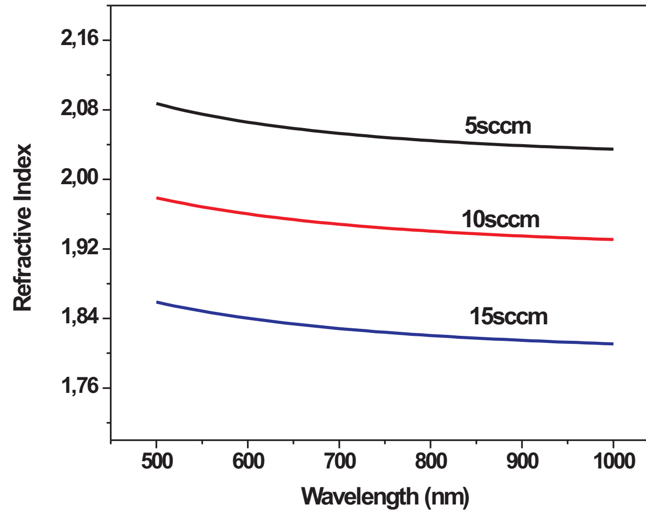

Figure 2.8: Refractive index values of Si-rich silicon nitride film between 500 and 1000 nm.

2.2.3 Fabrication of Nanocrystal MOS Capacitors

The memory devices used in this study were MOS capacitors with a trilayer dielectric stack consisting of Si/Ge nanocrystals sandwiched between a tunneling and a capping SiO_2 layers. The n and p-type Si substrates with a resistivity of 1-10 Ωcm were cleaned by Piranha process followed by dipping in dilute HF for 1 min to remove the native oxide from the surface. Back side metalization was done by 10 nm of Titanium (Ti) and 50 nm of gold (Au) evaporation. To have a high quality ohmic contact, samples were subjected to rapid thermal annealing (RTA) in forming gas (5 % H_2 and 95 % N_2) at 500 ^oC for an optimized annealing time of 60 s. Then, a tunneling oxide layer of thickness 4 nm was grown on Si substrate by dry oxidation. The intermediate layer, containing of Si-ncs or Ge-ncs, was then deposited by PECVD method as explained previously. The thickness of the nanocrystal layer was 10 nm. The Si-rich silicondioxide and germanosilicate

samples were then annealed in N_2 atmosphere in an alumina oven at 1200 ^oC for 1 hour and between 650-850 ^oC for 5 minutes, respectively. Finally, the top oxide layer (20-25 nm thick) was deposited by PECVD method. After defining the 1x1 mm capacitors by optical lithography, front side ohmic metalization was done by 10 nm of Ti and 50 nm of Au evaporation. As a last step, the samples were put into acetone solvent for lift-off process. The fabrication steps are given Figure 2.9.

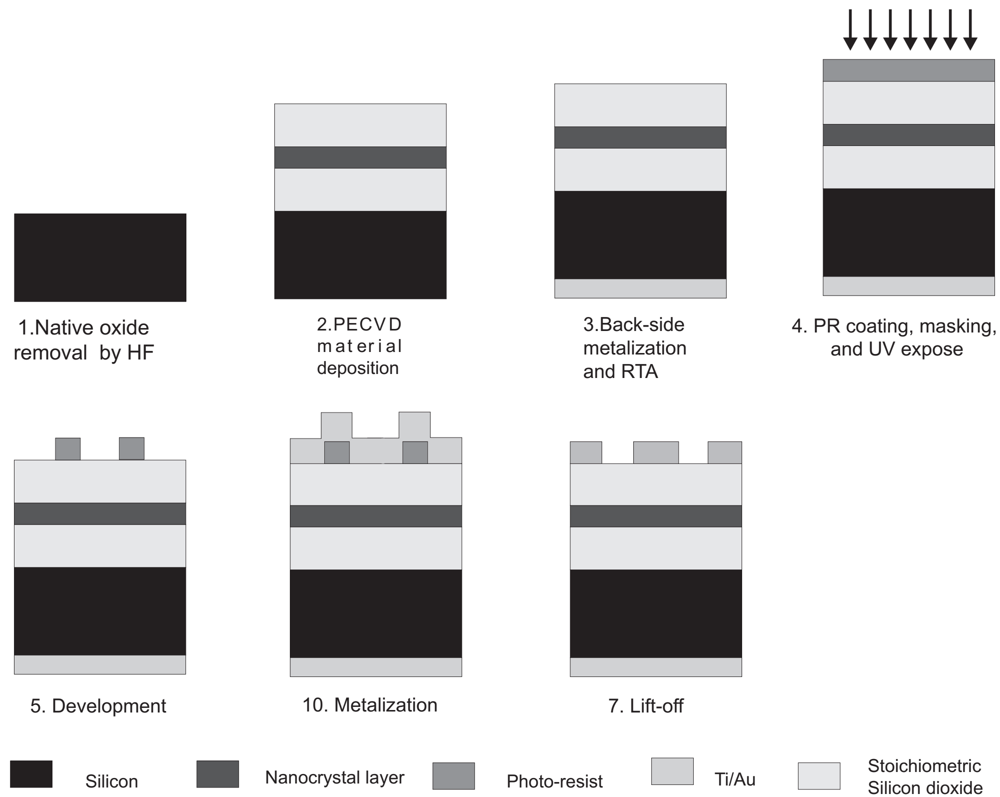

Figure 2.9: Nanocrystal MOS fabrication fabrication steps.

In samples where it was desired to obtain a well controlled thickness gradient, during PECVD material growth process, a glass barrier was placed over the silicon substrate. This procedure was not applied to all samples, but for some of them to observe the effect of film thickness on the storage and escape of electrons and holes. Using this method, device optimization can be made very quickly for PECVD grown devices. Schematic representation of this growth method is given in Figure 2.10.

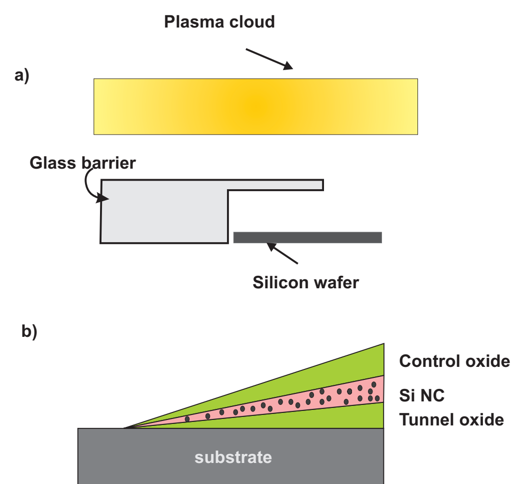

Figure 2.10: **(a)** A glass barrier is placed over a part of the silicon substrate for shielding the plasma. Under this barrier no material growth is observed. **(b)** This figure illustrates the structure of the sample after PECVD gradient growth method.

Chapter 3

Modelling of Nanocrystal MOS Capacitors

3.1 Fundametals of MOS Capacitors

The nanocrystal memories that we have produced were basically metal-oxide-semiconductor (MOS) capacitors. To understand the operation mechanism of the nanocrystal flash memories, one has to know the operation mechanism of MOS capacitors. A typical MOS structure with silicon nanocrystal floating gate is given in Figure 3.1.

There are four different modes of operation for a MOS structure which are accumulation, depletion, flat-band, and inversion.

Accumulation

Accumulation occurs when a voltage less than the flat-band voltage,V_{FB}, is applied. The negative charges on the gate attracts holes from the substrate to the oxide-semiconductor interface. In the case of nanocrystal floating gate MOS capacitors, the electrons inside the nanocrystals are detrapped and holes are accumulated. Only a small amount of band bending is needed to build up the

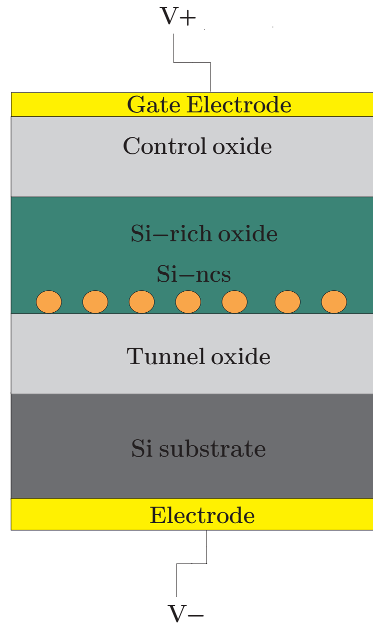

Figure 3.1: A MOS capacitor structure with Si-ncs are used as floating gate.

accumulation charge. The schematic illustration of charge transport and band-diagram during the accumulation operation of Si-nc MOS capacitors is given in Figure 3.2.

Depletion

Depletion occurs for positive voltages. When a positive voltage is applied to the gate, the holes in the semiconductor close to the gate are repelled by the positive charge on the gate, and they exit the device from bottom contact. They leave behind a depleted region which is insulating due to the absence of mobile carriers. The depletion layer width further increases with increasing gate voltage until oxide breakdown occurs.

Deep depletion refers to widening of the depletion layer beyond its thermal equilibrium width. Deep depletion can also occur in thin oxide MOS capacitors, with oxide thickness less than 5 nm. In such devices an inversion layer cannot form because minority carriers tunnel through the oxide to the gate electrode and consequently, deep depletion occurs.

Inversion

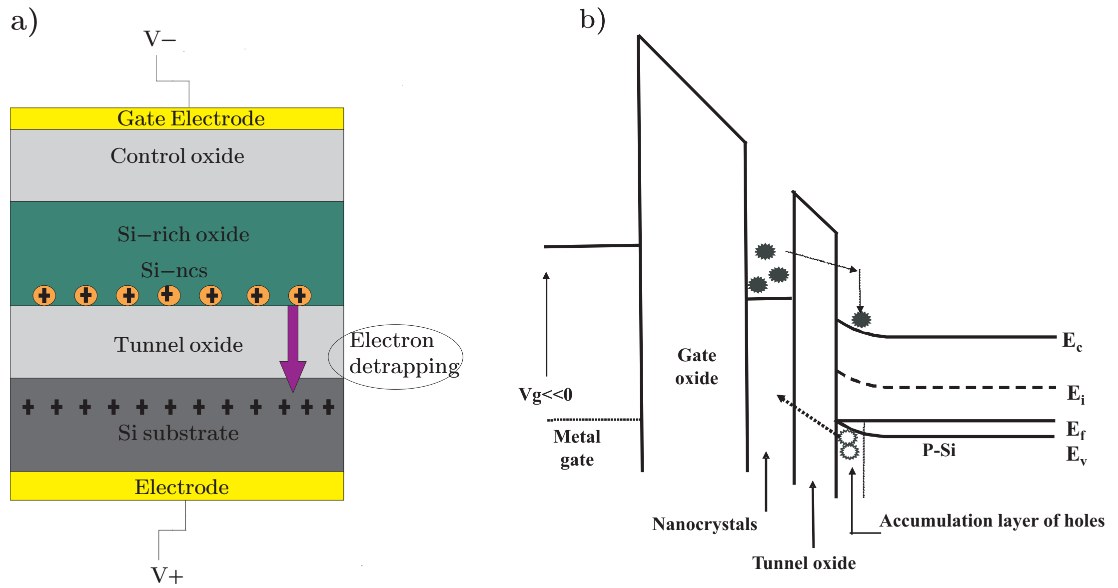

Figure 3.2: **a)**During accumulation, electrons detrapped from nanocrystals with the applied positive gate voltage.**b)**

Inversion occurs at voltages beyond the threshold voltage. Negative charges inside the substrate are attracted by the positive gate voltage and a negatively charged inversion layer at the oxide-semiconductor interface is formed. In the case of Si-nc MOS structures, electrons are trapped inside the nanocrystals. The schematic representation of charge transport and band diagram during the inversion operation of nanocrystal MOS capacitors is given in Figure 3.3

Flat-band

When there is no charge in the semiconductor, the energy band diagram becomes flat, this is referred as flat-band. The voltage separating the accumulation and depletion regime is called as flat-band voltage, V_{FB}. The flat band voltage is obtained when the applied gate voltage equals the work-function difference between the gate metal and the semiconductor. If there is also a fixed charge in the oxide and/or at the oxide-silicon interface, the expression for the flat-band voltage must be modified accordingly.

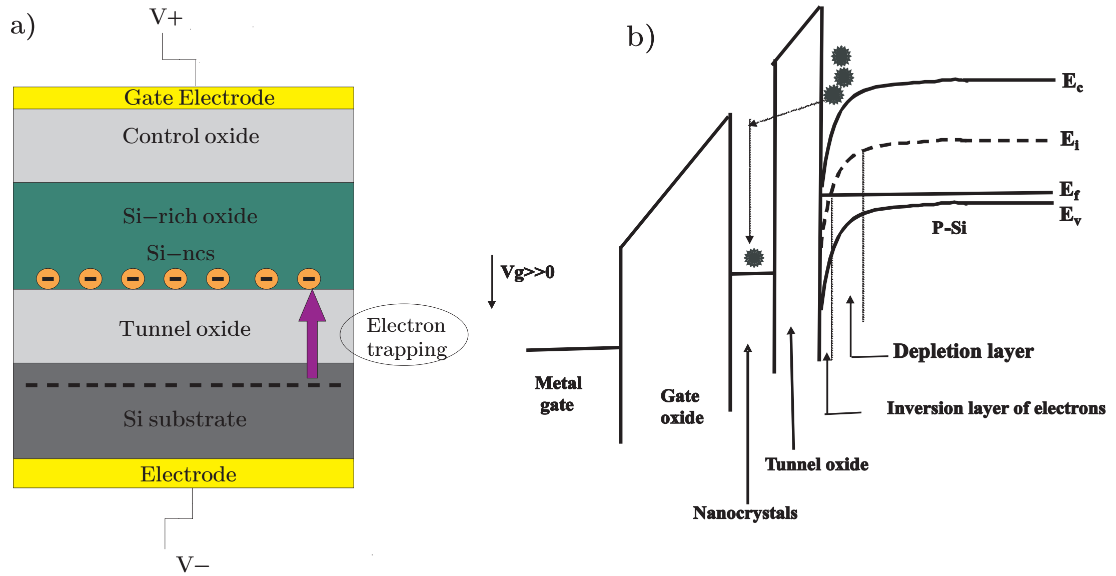

Figure 3.3: During inversion electrons trapped inside the nanocrystals by applying negative positive voltage to the gate electrode.

3.2 Basic Conduction Mechanisms for MOS Capacitors

Most amorphous insulators under an electric field show a range of nonlinear current-voltage dependence, and can be interpreted based on certain conduction mechanisms. The fundamental mechanisms in the description of the current-voltage (I-V) characteristics of a MOS structure are Fowler-Nordheim (FN) and direct tunneling.

Fowler-Nordheim Tunneling

FN tunneling has been studied extensively in MOS structures where it has been shown to be the dominant current mechanism, especially for thick oxides ($>$ 4 nm)) [42]. The basic idea is that quantum tunneling of carriers occurs through a triangular potential barrier in the presence of a high electric field as shown in Figure 3.4.

The barrier of the insulator is pulled down by the electric field and as a result electron tunneling from the metal Fermi level into the oxide conduction band

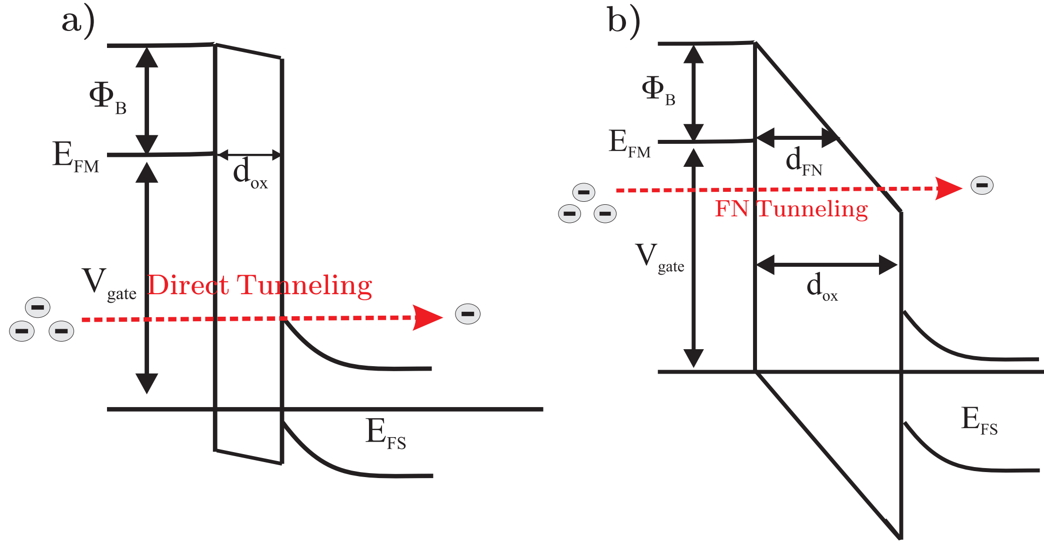

Figure 3.4: Schematic representation of the Fowler Nordheim tunneling under high voltage. In here Φ_B barrier height, E_{FM} metal Fermi level, E_{FS} semiconductor Fermi level, d_{ox} oxide thickness, d_{FN} tunneling distance, and V_{gate} gate voltage

becomes possible. To check whether the leading current mechanism in the device is FN tunneling, I-V data is typically plotted as $\ln(J_{FN}/E_{ox}^2)$ - $1/E_{ox}$, a so-called Fowler-Nordheim plot. FN tunneling is worked under high electric field, therefore using the FN tunneling to in charge/discharge operations will result in defects or carrier accumulation, and eventually breakdown occurs [42].

Direct Tunneling

In the simple case for oxide thickness smaller than 2 nm, direct tunneling dominates, the electrons pass through the full oxide thickness and the gate current is due to direct tunneling [19]. The graphical representation of direct tunneling mechanism and corresponding band diagram is given in Figure 3.4.

Direct-tunneling regime enables fast and low voltage operations but is limited by charge loss in the continuous floating gate. The probability of direct tunneling is a very strong function of the width of the barrier that electron tunnels through (oxide thickness in MOS devices).

3.3 Fundamentals of Nanocrystal MOS capacitor

In [27], it is assumed that, only nanocrystals are responsible for charge/storage and a single electron is stored in a nanocrystal. Based on these assumptions flat-band voltage shift can be written as:

$$\Delta V_{FB} = \frac{qn_{nc}}{\epsilon_{ox}}(t_{ox} + \frac{\epsilon_{ox} t_{nc}}{2\epsilon_{ge}}) \simeq \frac{qn_{nc}t_{ox}}{\epsilon_{ox}} \tag{3.1}$$

where q is the electronic charge, t_{ox} is the total oxide thickness including control and tunnel oxides, t_{nc} is the average diameter of the nanocrystals, ϵ's are the dielectric constants of respective materials.

To understand dynamical properties of memory elements, charging and discharging currents must be calculated taking into account tunnelling through the barrier for a given electric field within the tunnelling region. The currents also depend on availability of initial and final states. Since there are many device parameters that determine the charge-discharge currents, obtaining an analytical formula is difficult. Therefore, in the following charge, discharge and erase currents are studied separately, and appropriate formulas are given whenever possible.

3.3.1 Charging of Nanocrystal MOS capacitors

We try to model charging with the simplest approach. During the write cycle, the device is in accumulation and initially there is no stored charge in the device. In this case, the oxide field F_{tox} will be determined by the gate voltage V_{gate} approximately as $F_{tox} \simeq V_{gate}/t_{ox}$, where t_{ox} is the total oxide thickness.

For calculating the tunnelling current through a trapezoidal barrier, two limits in terms of applied field can be used. High-field limit is occurred when the voltage drop across the barrier is greater than the unperturbed barrier height. This results

in the well known Fowler-Nordheim current. When the tunneling oxide is very thin, the direct tunnelling limit is observed. In direct tunneling the voltage drop across the barrier is smaller than the original barrier height. Since, low voltage operation is desired in flash memory devices, we assume low fields and calculate direct tunnelling currents for the charging case. In this case, the charging current density becomes [17].

$$J_c = \frac{AF_{tox}^2}{V_B} \times \exp[-(1-(1-\frac{F_{tox}t_{tox}}{V_B})^{3/2})\frac{BV_B^{3/2}}{F_{tox}}] \tag{3.2}$$

where $A = q^2 m_{si}/16\pi^2 m_{ox}\hbar$, $B = 2\sqrt{8m_{ox}q}/3\hbar$, F_{tox} is the tunnel oxide field during charging, m_{ox} is the tunnel effective mass and V_B is the barrier height between the oxide and the substrate.

The availability of the final states will determine the deposited actual charge. Using a capture cross section per nanocrystal, this problem can be solved. The differential charge deposited per unit area $d\sigma$ in a time interval $d\tau$ can be calculated as:

$$d\sigma = p_c D_{trap} J_c(F_{tox}) d\tau \tag{3.3}$$

where p_c is the average capture cross section, and D_{trap} is the available density of final states. The capture probability may depend on nanocrystal shape.

3.3.2 Discharging of Nanocrystal MOS Capacitors

During retention, the device is in depletion and $V_{gate} = 0$. If we assume that the nanocrystal bound states are responsible for storage of carriers, the discharge of the electrons occurs by tunnelling from the nanocrystal ground state to the substrate, either by direct or trap assisted tunnelling. For the case of direct tunnelling, the current density describing the discharge of the nanocrystals is different than Eq. 3.2 because initial states are nanocrystal states instead of

bulk states. Assuming a delta-function distribution for the nanocrystal states $D_{NC}(E) = N_{NC}\delta(E - E_{NC})$ located at the quantization energy of E_{NC} and a single stored carrier for every nanocrystal, the discharge current density can be given as

$$J_d = qN_{NC}T_t(E_{NC})\nu_{NC} \tag{3.4}$$

where $\nu_{NC} \simeq \hbar\pi/2m_{ge}d^2$ is the semi-classical escape attempt rate for NCs of diameter d [36].

The transmission probability $T_t(E, F_{tox})$ for a single electron at energy E can be calculated through the WKB approximation as

$$T_t(E) \approx 4\exp[-(1-(1-\frac{F_{tox}t_{tox}}{V_B(E)})^{3/2})\frac{BV_B(E)^{3/2}}{F_{tox}}]. \tag{3.5}$$

The tunnel oxide field is determined by the amount of stored carriers as well as by the band-bending. For a given stored charge, the oxide field depends on the tunnel oxide thickness, total oxide thickness, substrate doping, gate work-function and dielectric constants. In order to obtain an appropriate result, we consider the case where stored charge is small and tunnel oxide field is proportional to the stored charge , $F_{tox} \approx \Delta V_{FB}/2t_{ox}$.

For the calculation of the discharge current through Eqs. 3.4 and 3.5, the barrier height must also be calculated. The barrier height is a function of the nanocrystal ground state energy given by $V_B(E) = V_{B0} - E_{NC}$, where V_{B0} is the bulk barrier height. The conduction band minimum of Ge NCs as a function of size is given by [35]

$$E_{CBM}(d) = E_{CBM}(\infty) + \frac{11.86}{d^2 + 1.51d + 3.3936} \tag{3.6}$$

where the energies are in eV, d is the nanocrystal diameter in nm. Eq. 3.6

can be used to estimate E_{NC}, which can be used in the estimation the tunnelling barrier observed by the nanocrystals during discharge.

The size distribution of nanocrystals leads to a distribution of energies. Considering the finite width of size distribution, using a broadened density of states is more appropriate than using delta function distribution. In this case, the stored charge is distributed to the available nanocrystal states according to a Fermi-Dirac distribution.

Assuming thermal equilibrium within the nanocrystal layer, the distribution of carriers to available states and the quasi-Fermi level can be calculated for a given total stored charge. In this case, for a given total areal density of N_{NC}, the total number of stored carriers is given by

$$n_c = \frac{N_{NC}}{\sqrt{2\pi}\sigma_E} \int \frac{\exp[-(E - E_{NC,ave})^2/2\sigma_E^2]}{1 + exp[(E - E_{F,NC})/k_B T]} dE \tag{3.7}$$

where $E_{NC,ave}$ is the average nanocrystal ground state energy, $E_{F,NC}$ is the quasi-Fermi level of the nanocrystals layer, and σ_E is the half-width of the nanocrystals energy distribution.

The quasi-Fermi level is a weak function of temperature, but depends strongly only on the ratio of total stored charge to number of nanocrystals. Therefore, for a given flat-band voltage shift, the quasi-Fermi level depends on the nanocrystal density, and average ground state energy of the nanocrystals. Escape of carriers near or above the quasi-Fermi level dominates the discharge current. Therefore, discharge current depends on the number of stored carriers which is proportional to the flat-band voltage shift.

A simple formula for the discharge current is desirable to compare the effect of design parameters on charge retention. However, simple expression for the quasi-Fermi level and tunnelling current can not be obtained without further simplifying assumptions. A simple formula can be obtained by assuming a rectangular shaped density of states, neglecting band bending effects, assuming a gate work-function that is aligned with the substrate Fermi level and calculating

in the zero temperature limit. Under these assumptions, Eqs. 3.4, 3.5, and 3.7 can be used to derive a simple formula for the discharge current at zero gate bias.

The discharge current is then given as a function of the flat-band voltage shift ΔV_{FB} due to stored carriers as

$$J_d \simeq \frac{4qN_{NC}\pi\hbar\sqrt{V_p}\exp[-\frac{3}{2}Bt_{tox}\sqrt{V_p}]}{3m_{ge}d^2Bt_{tox}\sigma_E} \times \{\exp(\frac{3Bt_{tox}\sigma_E}{2\sqrt{V_p}}\frac{\Delta V_{FB}}{\Delta V_{max}}) - 1\} \qquad (3.8)$$

where $V_p = V_B - E_p/q$ is the barrier height observed by the average size nanocrystal, σ_E is the width of the rectangular energy distribution, t_{tox} is the tunnel oxide thickness, m_{ge} is the electron mass in the nanocrystal, $\Delta V_{max} \simeq qN_{NC}t_{ox}/\epsilon_{ox}$ is the maximum flat-band voltage shift when all nanocrystals carry an electron, and $B = 4\sqrt{2m_{ox}q}/3\hbar$, m_{ox} being the electron tunnelling mass. Note that V_p and σ_E are normalized by q, to have units of Volts.

If carriers are stored in deep traps associated with nanocrystals, the discharge model is significantly different than the nanocrystal storage case. Models describing retention of carriers in traps have been described in previous studies [10]. In this case, the barrier observed by the stored carriers is larger than that observed by those stored in the nanocrystal ground level. Therefore, the escape of carriers rely on de-trapping by thermal excitations. However, once de-trapping occurs, the discharge current density will be similar to that given in Eq. 3.8.

Chapter 4

Electrical Characterization of Nanocrystal MOS Capacitors

4.1 Germanium Nanocrystal MOS Capacitors

The electrical characterization of the devices consists of three steps: flat-band voltage measurements, charging of nanocrystals and discharging of nanocrystals. High frequency capacitance-voltage (C-V) measurements are the common part of these measurement techniques. High frequency C-V measurement technique is explained in the following.

4.1.1 High Frequency Capacitance-Voltage Measurements

To understand capacitance-voltage measurements one must first be familiar with the frequency dependence of the measurement. This frequency dependence occurs in inversion. High- and low-frequency C-V measurements are often useful among various methods to evaluate the MOS characteristics. Most capacitance measurements are performed with admittance bridges or capacitance meters. Using

Gauss law, the small-signal equivalent circuit of the MOS capacitor was derived as follows [37]:

$$\frac{1}{C} = \frac{1}{C_{si}(\phi)} + \frac{1}{C_{ox}} \tag{4.1}$$

Above equation expresses the total capacitance per unit areas of the MOS capacitor as the series combination of the silicon capacitance per unit area and the oxide capacitance per unit area.

The high frequency capacitance is used to evaluate the fixed-charge density and doping density. The low frequency capacitance is conventionally used to evaluate the interface-state density and surface potential [[37]]. At high frequency, typically 0.1- 1 MHz, majority carriers respond instantaneously. Interface traps do not contribute to the high frequency C-V curve, since they do not respond to the ac gate voltage. On the other hand, they follow very slow changes in gate bias as the mode of operation is changed from accumulation to inversion.

4.1.2 Flat-band Voltage Measurements

Capacitance measurements were performed using a capacitance meter (HP 4278A) at 1 MHz AC excitation with 25 mV amplitude. The flat-band voltage shift can be tracked quasi-real-time for small changes in the flat-band shift by using a digital feedback loop that was developed in our laboratory. The feedback loop is used to measure flat-band voltage shifts before and after applied pulses or during retention. During write/erase pulses, the loop can be momentarily turned off, and after the pulse it can be restarted at the same bias voltage. This method allows rapid monitoring of the changes in the flat-band voltage shift after a write or erase pulse. The flat-band voltage difference can be measured rapidly and can be used to extract the discharge or charge currents.

Noting that, the derivative of the flat-band voltage shift divided by pulse duration gives the charge current density, we plotted the charging current per

nanocrystal in Figure 4.1. It is seen that, for small charging currents, charging current increases monotonically with annealing temperature for n and p type samples.

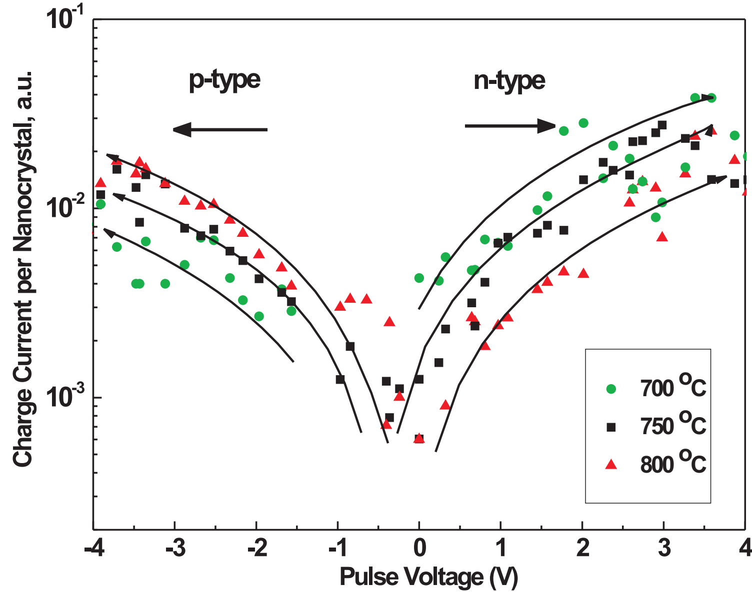

Figure 4.1: Experimental data of charging of n (right) and p (left) type capacitors. Charging currents as a function of charge voltage are measured for samples annealed at 700-800 ^oC.

It is observed that, for voltage pulse amplitudes of less than 4 V, the charge currents for electron and holes are roughly on the same order of magnitude, electrons tunneling faster by less than a factor of three than holes, since hole barrier is greater when SiO_2 is used as the tunnel dielectric.

4.1.3 Charging of Nanocrystals

To investigate the trapping characteristics of the structure we performed high frequency (1 MHz) C-V measurements for Ge-nc MOS structures. The samples were charged to 3 V by applying 10 V of initial pulse voltage. The measurements were carried out using a HP 4278A impedance analyzer. Due to the ability of storage and trap-detrap processes of carriers in Ge-ncs embedded in the dielectric matrix, we can describe the properties by high frequency C-V curves.

4.1.4 Discharging of Nanocrystals

The discharge currents have been measured in the same setup by monitoring the flat-band voltage shift as a function of time. For decay measurements, first, Ge-nc MOS capacitors were charged to 3 V under 10 V of initial pulse voltage. Then pulse voltage was turned off and the decay of stored charge as a function of time was measured. The derivative of the flat-band voltage shift was calculated numerically and plotted as a function of time in Figure 4.2.

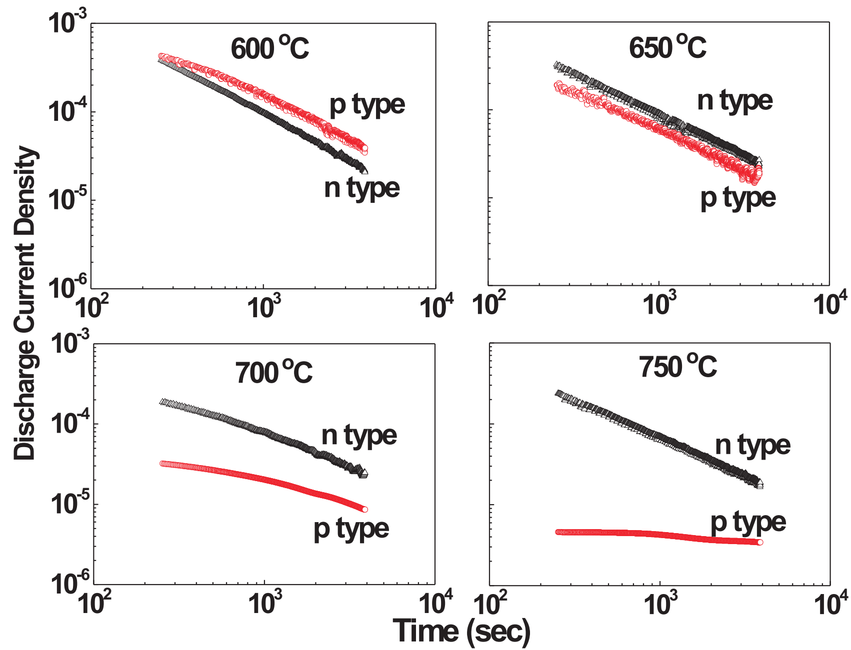

Figure 4.2: Discharge current densities as a function of time for n and p type devices (in terms of substrate types). The holes decay faster than the electrons for samples annealed at low temperatures whereas they decay much slower for samples annealed at higher temperatures.

It is seen that, the discharge currents of holes are larger than that of electrons for a similar flat-band voltage shift at low annealing temperatures. However, as the annealing temperature is raised, hole escape rates drop below those of the electrons, the difference becoming larger at higher annealing temperatures.

As the direct tunneling current is normally expected to be weak, surprisingly high hole discharge current at low annealing temperatures suggests that hole

discharge dynamics are dominated by other mechanisms than direct tunneling such as trap assisted tunneling. On the other hand samples annealed at higher temperatures show very low escape times for holes. This suggests that there is significant trapping of holes during the discharge phase. This could be understood by considering two factors that come into play at higher annealing temperatures. First, as the temperature is raised, nanocrystal sizes increase which in turn results in a higher energy barrier for holes bound at quantum states of the nanocrystal. Second, the diffusion of Ge to the interface should result SiGe alloy formation which constitutes a quantum well. This results in more homogeneous layer with less interface states. In addition, on their way to the substrate, holes encounter with the SiGe quantum well and they are trapped at the bound states of the quantum well. Increased annealing temperatures result in longer diffusion lengths for Ge hence wider quantum wells and larger barriers for holes trapped in the quantum well.

The results are summarized in the schematic band diagram for electrons and holes in Figure 4.3. Note that at low annealing temperatures, Ge atoms diffusing to the interface do not form a homogeneous layer. However, they create significant amount of interface trap states in the band gap of Si near the valence band edge lie energetically close to the confined states of holes in Ge-ncs in contrast with electron confined states which are above the conduction band edge. It can be argued that, both the valance band states, and the presence of large number of traps within the silicon band gap result in an increased discharge current, mainly due to trap assisted tunneling of holes. As the annealing temperature is raised, the energy band diagram is modified by the presence of a thin quantum well at the oxide Si interface and the presence of larger nanocrystal sizes. It should be noted that, introduction of Ge into Si does not change the conduction band appreciably while the valence band is raised. This is the reason for the different behavior of holes than electrons.

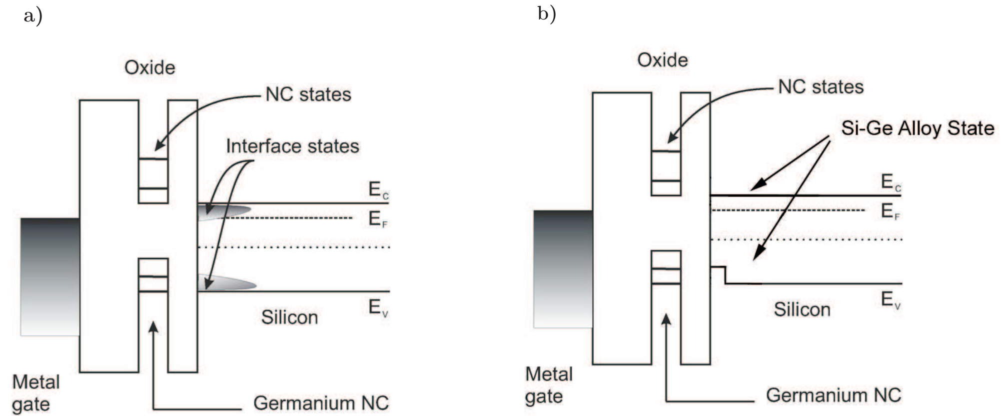

Figure 4.3: Band structure of Ge nanocrystal MOS capacitor, a) annealed at low temperatures, b) annealed at high temperatures. Note the effect of quantum well at the interface and the increased nanocrystal size.

4.2 Silicon Nanocrystal MOS Capacitors

The gradient growth method was used in Si-nc MOS capacitor fabrication. Different samples were fabricated by putting the glass barrier on top of the different layers. In here, MOS capacitors with gradient nc-layer and gradient tunnel oxide layer were fabricated. Moreover, stoichiometric and gradient free samples were fabricated for comparison.

4.2.1 Flat-Band Measurements

Flat-band measurements were performed using a capacitance meter (HP 4278A) at 1 MHz AC excitation with 100 mV amplitude. The effect of tunnel oxide thickness on the flat band voltage shift was studied. From flat-band voltage measurements for each sample different types of charge motions were observed.

The sample presented in Figure 4.5 was prepared by using 200 sccm of SiH_4, 180 sccm NH_3 at 350 ^oC, by applying the gradient growth method to the tunnel oxide layer.

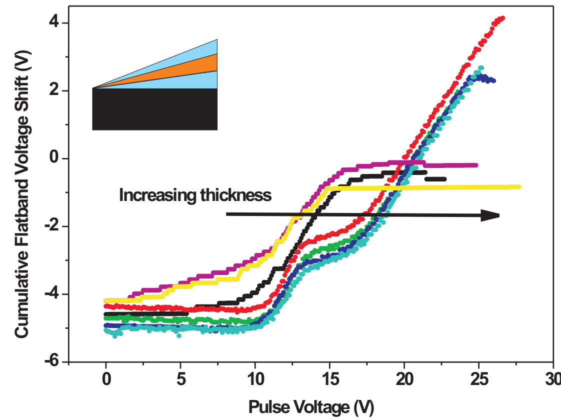

Figure 4.4: Cumulative flat-band voltage shift as a function of pulse voltage. Tunnel oxide layer was grown by gradient growth method. The dip beyond 15 V indicates the in-layer charge motion.

It is seen that, in-layer charge motion was observed with increasing tunnel oxide thickness and beyond 15 V of pulse voltage, it became significant for thicker samples. This charge motion corresponds to a negative hysteresis.

The sample that has the gradient in nanocrystal layer that was fabricated under the same process conditions also behaved similar with the previous one and at 15 V of pulse voltage in-layer charge motion was observed. With the increasing thickness the number of charges that transport became more significant which is given in Figure 4.5.

The sample seen in Figure 4.6 was prepared using 450 sccm of SiH_4, 200 sccm of NH_3. Gradient growth method was not used. Beyond the pulse voltage of 10 V, motion of the residual charges in the nanocrystal layer was observed. Between 15 and 20 V, oxide-nitride interface states were charged and at 20 V interface charges were transfered to the nanocrystal layer.

The effect of nanocrystals on charge motion was studied on a stoichiometric sample which was fabricated using 180 sccm SiH_4, 200 sccm NH_3. Gradient method was used during the nanocrystal layer deposition. States at the oxide-nitride interface may be charged but in-layer charge motion was not observed in this sample as it is given in Figure 4.7.

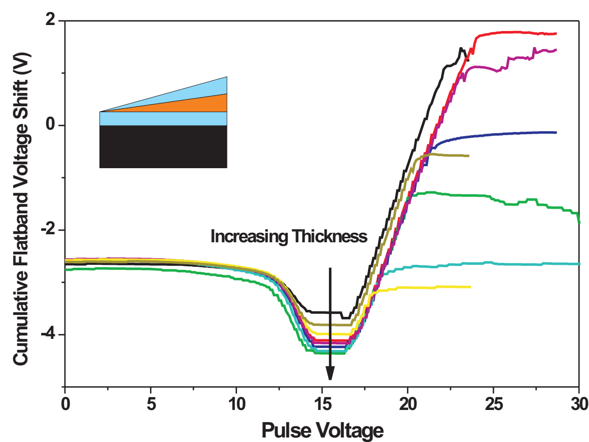

Figure 4.5: For this sample gradient growth method was applied to the nanocrystal formation layer. At 15 V of pulse voltage in-layer charge motion is seen which corresponds to a negative hysteresis.

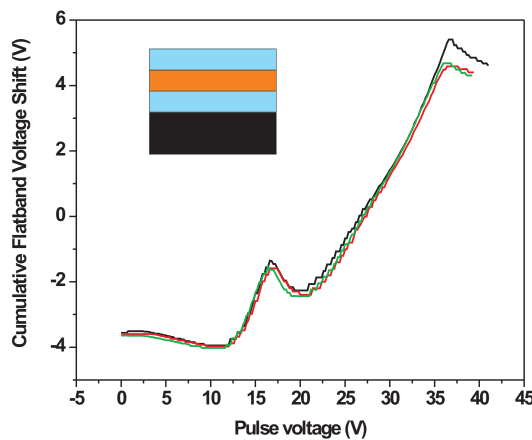

Figure 4.6: Cumulative flat-band voltage shift of the sample which was not grown by gradient growth method. Charge motion is observed inside the nanocrytstal layer and at the oxide-nitride interface at specific voltages.

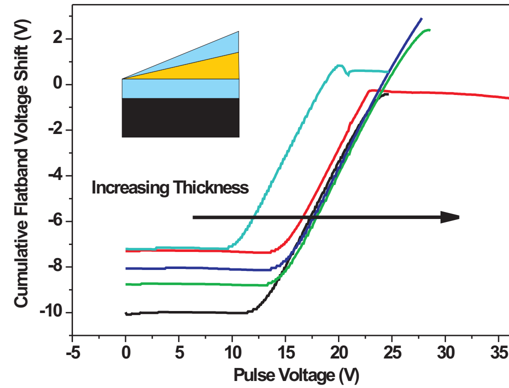

Figure 4.7: Cumulative flat-band voltage shift of the stoichiometric sample as a function of the pulse voltage. Note that there is no in-layer charge motion for this sample.

4.2.2 Charging of Nanocrystals

High frequency (1 MHz) multiple up-down C-V sweeps between inversion and accumulation region were conducted for our Si-nc MOS devices. The capacitor structures were charged to 3 V by applying 10 V of initial pulse voltage. The measurements were carried out using a HP 4278A impedance analyzer in a dark box for avoiding photocurrent.

When the gate electrode is in writing operation the charges are stored in the Si-nc by Fowler-Nordheim tunneling through the thin oxide, and in the erase operation, a number of charges will be able to escape from the Si-ncs, and the neutral charge state is achieved again. The whole sweep process results in a shift of the capacitance.

4.2.3 Discharging of Nanocrystals

For decay measurements first, Si-nc MOS capacitors, with a gradually increasing tunnel oxide layer, were charged to 3 V under 10 V of initial pulse voltage. Then pulse voltage was turned off and the decay of stored charge was measured. The

results are given in Figure 4.8.

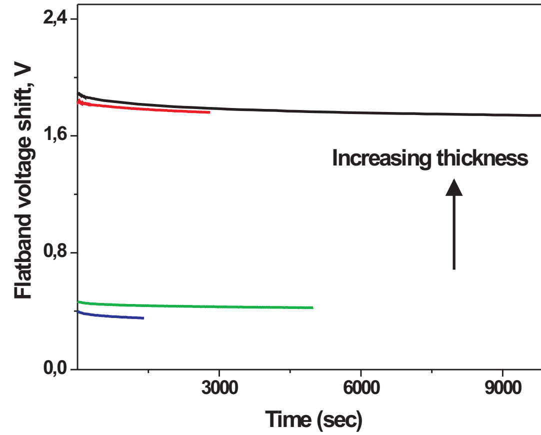

Figure 4.8: Decay of the stored charges of the Si-nc MOS capacitors which has a gradually increasing layers. With increasing thickness decay rate of the charges decreases.

As can be seen from the Figure 4.8, the capacitors with a thicker tunnel oxide store the charges for a longer time. Discharge current decreases with the increasing thickness of the tunnel oxide, therefore the charge retention time increases.

4.3 Conclusions

In conclusion, we have studied charge and discharge dynamics of both electrons and holes in PECVD grown and post annealed Ge-nc MOS capacitors. We found that hole retention times are actually shorter than electron retention times for samples annealed at low temperatures. We suggested that the observed reduction of hole retention times is due to interface traps states. However, formation of a Ge rich alloy at the interface with high temperature annealing results in longer retention times, which is promising for actual device operations. These observations emphasize the importance of proper interface engineering for Ge-nc memory devices.

Moreover, the silicon nanocrystal-based MOS memory devices with smoothly

varying layer thicknesses were fabricated by using PECVD gradient growth method. These structures were characterized for charge motions inside the nanocrystal layer and at the oxide-nitride interface.

Most of the results presented in this chapter have been published in [2].

Chapter 5

Electro-optic and Electro-absorption Properties of InAs Quantum Dot Waveguides

5.1 Introduction

InAs quantum dots are well known for many interesting optical and electrical properties. They are grown on GaAs by molecular beam epitaxy. Deposition of several mono-layers of InAs on GaAs results in the formation of quantum dots due to the lattice mismatch between InAs and GaAs. A major achievement is the realization of quantum dot lasers. Many properties of InAs quantum dots have been studied while very little is known on the electro-optical (EO) properties of these quantum dots. Both electro-optic effects and electro-absorption (EA) are important parameters that are crucial in the design and realization of many active optical devices.

In the literature there is limited data on EO and EA effects in quantum dots. Furthermore, little has been reported on the voltage dependent modulation of quantum dot embedded waveguides [18, 11].

Davis et al. have measured the electro-optic coefficient of lithographically defined $In_{0.15}Ga_{0.85}$As quantum boxes embedded in optical waveguides at 1.15 μm using the phase retardation technique. They found 4.5 times increment in electro-optic coefficient when compared with GaAs [11].

Using the phase retardation technique, Ghosh et al. and Qasaimeh et al. have measured both linear and quadratic electro-optic coefficients at 1.15 μm of self organized $In_{0.40}Ga_{0.60}As$ and InAs quantum dots. They have used single-mode ridge waveguide structures which were grown by molecular beam epitaxy with self-organized InAs and $In_{0.40}Ga_{0.60}As$/GaAs quantum dots in the guiding region. They have measured linear and quadratic electro-optic coefficients as $2.58x10^{-11}m/V$ and $6.25x10^{-17}m^2/V^2$, respectively,which are higher than bulk GaAs or quantum well structures. For InAs quantum dots, the measured linear and quadratic electro-optic coefficients were $2.43x10^{-10}m/V$ and $3.37x10^{-17}m^2/V^2$ [18, 41].

Using the same approach, electro-optic coefficients of self assembled InAs and In(Ga)As quantum dots were recently measured and enhanced electro-optic coefficients were reported. Tatebayashi et al. have worked on 1.3 mm self-assembled InAs/GaAs quantum dots grown by metal organic chemical vapor deposition technique. They have used phase retardation technique and obtained linear and quadratic electro-optic coefficients as $2.4x10^{-11}m/V$ and $3.2x10^{-18}m^2/V^2$, respectively [46].

Moreau et al. have investigated the Pockels effect of InGaAs/GaAs quantum dots in 1.5 μm telecommunication window. Again phase retardation method was used and the measured linear electro-optic coefficient is nearly $3.4x10^{-11}m/V$. Also a 35 % enhancement of the phase variation was achieved compared to that obtained in bulk GaAs waveguides [34]

In this chapter, measurements of both EO and EA properties of multilayer InAs/GaAs self-organized quantum dots will be presented. Transmission through Fabry-Perot resonators formed by two cleaved facets in waveguides at wavelengths of 1.3 μm and 1.5 μm to determine the electro-absorption properties of quantum dots in addition to electro-optical properties is used. This is in contrast with

previous work, where phase retardation method was exclusively used.

In the following, we first describe the fundamentals of electro-optical and electro-absorption effects and give examples of how the effects are used.

The Electro-optic Effect

The linear EO effect is defined as the change of material refraction index under the presence of an electric field. The application of an electric field causes the electrons, ions, and permanent dipoles to reorient, inducing an electric polarization. The induced polarization produces an anisotropy that creates a birefringence. The field-dependent birefringence modifies the optical polarization of a light wave propagating through the medium. The theory assumes that the change in the index of refraction with applied field is small and can be described by a series expansion in powers of the applied electric field.

The change in the indices of refraction under an applied field is given in tensor equation $\Delta(1/n^2) = RE$. In this formula $\Delta(1/n^2)$ is the change in the index of refraction for the elements of the tensor Δ, R is the tensor of electro-optic coefficients, and E is the vector of the applied electric field. There are six relevant indices of refraction from the index ellipsoid, three terms for the three principle directions (x, y, and z), and three cross terms. An electric field has x, y, and z components, so in general this effect is described with a 6 x 3 tensor, R. Each component $\Delta(1/n^2)i$ for 1 < i < 6 is the dot product of the i-th row of R with the electric field vector. In non-electrooptic crystals (centrosymmetric), all of the terms r_{ij} are zero. Therefore, only non-centrosymmetric materials exhibit the linear electro-optic effect, also called the Pockels effect. Materials exhibiting the Pockels effect are called electro-optic materials. Materials such as potassium dihydrogen phosphate (KDP) and lithium niobate ($LiNO_3$) exhibit strong electro-optic coefficients [40].

All centrosymmetric media exhibit only the Kerr electro-optic effect, where the refractive index change is proportional to the square of the electric field strength, and is typically much weaker than the linear effect. Thus, applying an electric field on a waveguide will result in a change in the refractive index depending

on the crystal orientation relative to the electric field direction as well as on the magnitude of the elements of the electro-optic tensor. This effect can be used to design and fabricate electro-optic modulators [40].

An electro-optic modulator (EOM) is a device that can be used to modulate the amplitude, phase, direction, or frequency of the light wave under an applied electric field. The principle of operation is based on the linear electro-optic effect (Pockels Effect). Depending on the parameter that is modified, electro-optic modulators are classified as amplitude, phase, and polarization modulators [40].

Phase Modulators

The simplest type of electro-optic modulator is a phase modulator, where an electric field changes the phase delay of a light beam sent through the crystal. The polarization of the input beam often has to be aligned with one of the optical axes of the crystal, so that the polarization state is not changed. Many applications require only a small phase modulation. For example, this is often the case when one uses an EOM for monitoring and stabilizing a resonance frequency of an optical resonator.

Polarization Modulators

Depending on the type and orientation of the nonlinear crystal, and on the direction of the applied electric field, the phase delay can depend on the polarization direction. In polarization modulator system, the linear polarization of the light beam is altered by passing the beam through an electro-optic cell to which a modulation voltage has been applied. The cell converts the linearly polarized laser output to other kinds of polarization. For a particular value of voltage, a linearly polarized beam perpendicular to the original polarization is obtained, corresponding to 100% modulation.

Amplitude Modulators

Once one can make a phase modulating EOM, it's a simple matter to turn that into an amplitude modulating EOM by using a Mach-Zehnder interferometer. Simply one uses a beam splitter to divide the laser light into two paths, one of

which has a phase modulator, and then recombine the two beams. By changing the electric field on the phase modulating path, one can control whether the two beams constructively or destructively interfere and thereby control the amplitude or intensity of the exiting light.

The Electro-absorption Effect

Electro-absorption effect is defined as the change of material absorption in the presence of an electric field. It is called the Franz-Keldysh effect in bulk materials and Quantum Confined Stark Effect (QCSE) in quantum dot and quantum-well materials.

Franz-Keldysh electro-absorption effect can be described as the below-band-gap photon-assisted tunneling of electrons from the valence to the conduction band in the presence of the electric field. This effect is observed in bulk materials and it changes both the real and the imaginary part of the refractive index, but mostly the latter. Upon applying the electric field, the energy bands of the semiconductor experience a distortion, and this shifts the energy band gap which results in the absorption of the material particularly at wavelengths close to its band gap. So it is mostly dominant close to the material's band gap [40].

Electric field applied perpendicular to the multiple quantum dot or quantum well layers result in large shifts in the optical absorption to lower photon energies, with the exciton resonances remaining well resolved even at high electric field [40]. The excitons are not as easily field-ionized because there is a relatively long time period for the electrons and the holes to tunnel out of the quantum well, and the Coulomb attraction is strong since the electrons and holes are confined to the very thin quantum well region [40]. This electro-absorption effect in quantum dot and well structures is called Quantum Confined Stark Effect (QCSE).

In the case of QCSE, the absorption edge is much sharper and moves faster with reverse biased electric field as a result of this room temperature exciton resonance in MQW materials. This makes the MQW devices favorable in achieving low drive voltage, low insertion loss and high extinction ratio. In this chapter we will mainly concentrate on QCSE of InAs quantum dot structures to observe the

modulation characteristics under applied electric field.

5.2 InAs Quantum Dot Waveguides Under Applied Field

Much has been done to realize both EO and EA modulators in quantum wells using both Franz-Keldysh and quantum confined Stark effects. Quantum wells are observed with enhanced electro-optic effects due to the built-in birefringence and a quadratic electro-optic (Kerr) effect arising from the QCSE [24, 33]. Recently, advances in crystal growth have triggered the study of self organized quantum dots. Quantum dots are expected to exhibit enhanced optical nonlinearities and enhanced electro-optic effects due to the modification in their density of states since the ratio of optical nonlinearity of a quantum dot layer to that of a bulk material is proportional to a_B^3/V where a_B is the Bohr radius and V is the volume of the quantum dots [43, 45]. Since both EA and EO modulators require small size and low modulation voltages, possibility of obtaining quantum dots with enhanced electro-optic and/or electro-absorption coefficients makes them attractive for such applications.

Nonlinear optical and linear electro-optic materials find use in switching and modulation devices for photonic integrated circuits. For modulators in telecommunications small size and modulation voltages are desired. Both EO and EA modulators are candidates for use in external modulation links in telecommunications. These modulators can be realized using either bulk semiconductor materials [49] or materials with multiple quantum dots or wells [25].

5.2.1 InAs QD Waveguide Structures

We worked on waveguide structures containing three layers of quantum dots (3QDs) of lengths in the range of 1-1.6 mm. These structures were grown by molecular beam epitaxy to be used as quantum dot lasers. The active region

is formed by three layers of self-assembled InAs QDs, which are covered by a 5-nm $In_{0.15}Ga_{0.85}As$ QW and separated from each other by a 40-nm GaAs spacer layer. The areal dot density of our lens-shaped QDs is $3x10^{10}cm^{-2}$. The laser cavity is clad by 1.55 μm of $Al_{0.7}Ga_{0.3}As$, which is n-doped on the substrate side and p-doped on the top side. Our devices are single mode ridge waveguide structures with varying widths between 2-5 μm. Both facets are as cleaved. For each sample lasing is peaked at nearly 1285 nm [30]. Detailed structure and electroluminescence data are given in Figure 5.1.

Figure 5.1: EL data and detailed structure of the InAs quantum dot waveguides.

5.2.2 Measurement Set-up

Electro-optic and electro-absorption measurements were conducted by using the measurement set-up given in Figure 5.2.

In this set-up light is coming from a tunable laser source, which has a wavelength range of 1515-1560 nm(Santec Tunable LD Light Source TSL-520) and 1290-1360(Santec TSL-320 for 1300 nm) for electro-optic and electro-absorption measurements, respectively. Light is transmitted via single mode optical fiber and after passing the polarization control stage, TE polarized light is obtained. At the translational stage, the fiber and waveguide heights are aligned with respect to each other to obtain mode shape clearly with highest transmission power. Transmitted light is collected with an objective and pass through an aperture and

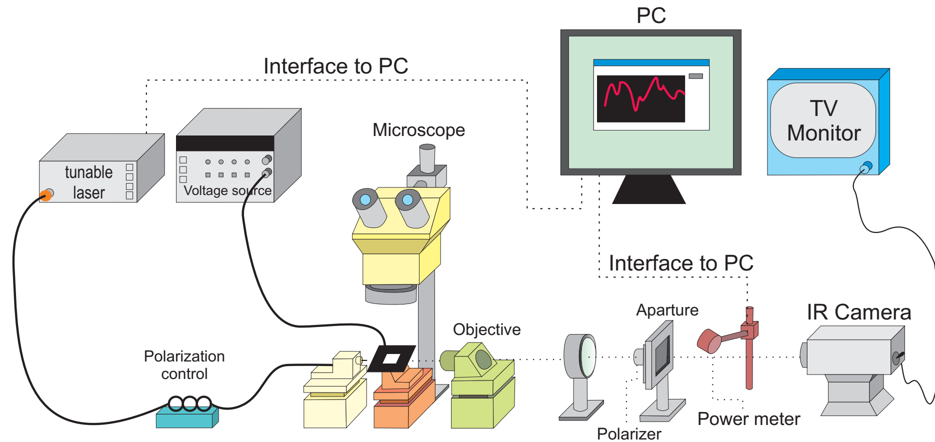

Figure 5.2: Measurement set-up for electrical and optical measurements.

polarizer combination. An infrared(IR) camera which is connected to a television monitor is used to observe the mode shape clearly. When the single mode propagation is obtained, a Ge detector is put in front of the IR camera and power of the transmitted light is measured. A DC voltage source is used to apply 0 to 20 Volt reverse bias to the samples. The detector is connected to a computer. The communication between computer and detector is controlled by a simulation program.

5.3 Simulations of InAs Quantum Dot Waveguides

Determination of the mode spectrum and mode profile of waveguides is essential in any optical waveguide structure. This also allows to determine the effective index as well as the confinement factor of the waveguides. Typically such simulations are done using commercial software packages based on finite difference or Fourier transform techniques. In this thesis, we used the finite difference simulator BeamProp from RSoft Inc. to simulate the waveguides under consideration. The finite difference simulator solves the paraxial equation given by:

$$\frac{\partial^2 U(x,y)}{\partial x^2} + \frac{\partial^2 U(x,y)}{\partial y^2} + {k_0}^2 \left[n(x,y)^2 - \tilde{n}^2 \right] U(x,y) \tag{5.1}$$

where U(x,y) is the transverse field amplitude, n(x,y) is the transverse index distribution and n is the background index. The optical wave propagates along the z direction. The whole structure is enveloped by a computation window large enough not to effect the results of the computation and appropriate boundary conditions are applied to eliminate spurious reflection signals for the boundaries. The waveguide is divided into mesh of grid points in all directions and at a given grid point along the z axis, computations are performed at each point on the transverse grid before moving onto the next grid point on the z axis. Partial derivatives in the paraxial equation, are approximated by using finite difference approach. This is done by expanding the equation via second order Taylor series of the field at adjacent grid points. As an example which when applied to the rest of the equation yields

$$\frac{U_j^{i+1} - 2U_j^i + U_j^{i-1}}{(\Delta x)^2} + \frac{U_{j+1}^i - 2U_j^i + U_{j-1}^i}{(\Delta y)^2} + k_0^2 \left((n_j^i)^2 - \tilde{n}^2 \right) U_j^i = 0 \tag{5.2}$$

This equation can be cast in the form of matrix equations whcih can be rapdily solved with computers. Simulations can be carried out in 2 or 3 dimensions and either for scalar or vector wave equations. Care was taken that the simulations were stable by choosing small grid sizes.

In the simulations, wavelength was taken as 1.515 μm and etch depth was 1.5 μm. For the InAs quantum dot waveguides, fundamental mode profiles of TE and TM polarizations are given in Figure 5.3, Figure 5.4.

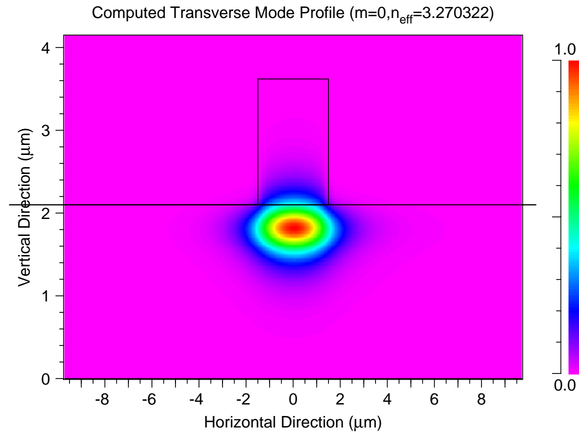

Figure 5.3: Fundamental mode profile of the InAs quantum dot waveguides for TE polarization. The effective index of the structure is obtained as 3.27 from simulation.

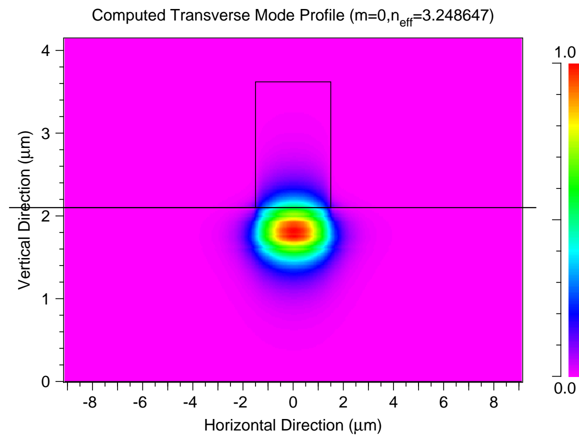

Figure 5.4: Fundamental mode profile of the InAs quantum dot waveguides for TM polarization. The effective index of the structure is obtained as 3.248 from simulation

5.4 Measurements and Results

5.4.1 Electro-optical Measurements

Measurement of the electro-optic coefficients at 1515 nm was carried out by coupling a TE polarized light from a tunable laser (Santec Tunable LD Light Source TSL-520) onto one end of the waveguide with a lens shaped fiber. A DC voltage source was used to apply 0 to 20 Volt reverse bias to the samples. The applied electric field was perpendicular to the quantum dot layers. At each voltage level, the transmission through the device was recorded as a function of wavelength and voltage. The details of the measurement set-up is given in the Figure 5.2.

Fabry-Perot resonances with large contrast were obtained and experimental data fitted well with the theoretical formula as shown in Figure 5.5. The well known Fabry-Perot transmission equation, given in Eq. 5.3, was used to fit measured data and mode effective index, loss coefficients, and a voltage independent phase factor were calculated based on this curve fitting.

$$T(\lambda) = \frac{T_0}{\left|1 - Ae^{-2j\left(2\pi n \frac{L}{\lambda}\right)+\theta}\right|^2} \tag{5.3}$$

where T_0 is the power transmission without any internal reflection, A is contrast ratio for the Fabry-Perot cavity, λ is the wavelength of interest, ϕ is the phase angle and n is the effective index.

Voltage dependent Fabry-Perot resonances are presented in Figure 5.6.

No voltage-dependent spectral shift is observed for TM polarization. This indicates that the quadratic electro-optic coefficient is not effective at this wavelength and that the linear electro-optic coefficient is dominated by the r_{41} component, similar to bulk. The linear electro-optic coefficient responsible for modulation is obtained using the mode effective index difference between two specific

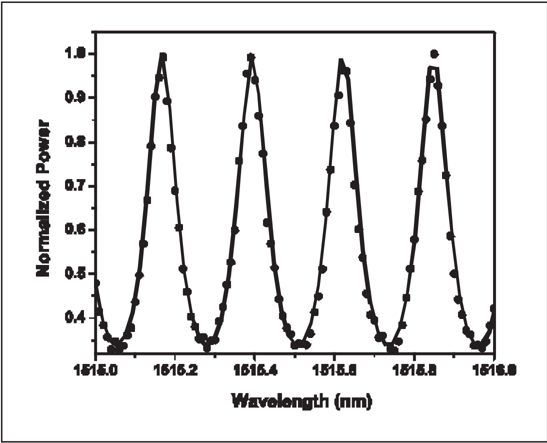

Figure 5.5: Fabry-Perot resonances at 1515 nm for 6 Volt reverse bias. The dots show the experimental data and the line indicates the optimum curve fit.

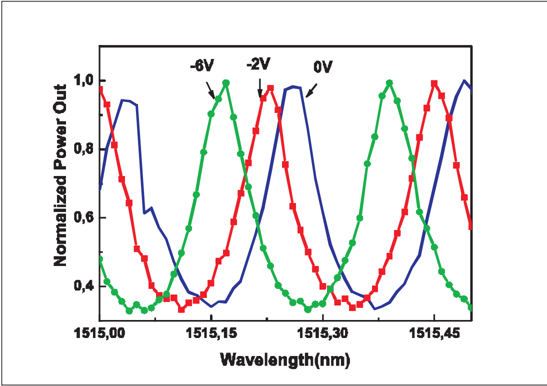

Figure 5.6: Voltage dependent shift of Fabry-Perot resonances. Significant tuning is observed with relatively low voltages.

voltages. The change in refractive index as a function of applied voltage is extracted from the data in Figure 5.6 and is shown in Figure 5.7.

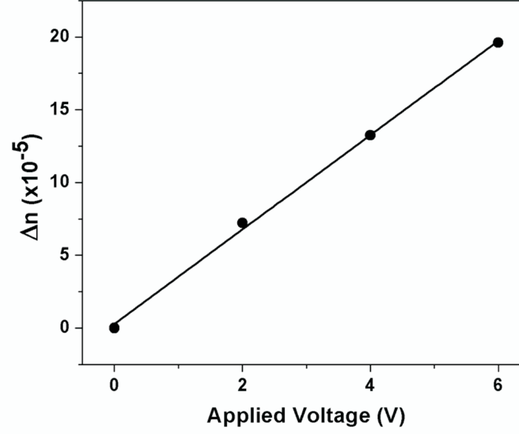

Figure 5.7: Variation in refractive index as a function of applied voltage at 1515 nm. The dots show the experimental data and the line indicates the linear fit.

The change in mode effective index varies linearly with the applied voltage and the maximum change is $2x10^{-4}$ for 6 Volt bias at 1515 nm. The change in the mode effective index due to applied voltage (Δn_e(V)) is given as [13]:

$$\Delta n_e\left(V\right) = \frac{1}{2}{n_e}^3 r_{41}\frac{V}{t}\Gamma. \tag{5.4}$$

where r_{41} is the electro-optic coefficient, t is the thickness of the undoped epilayer, n_e is the mode effective index, V is the voltage applied and Γ is the overlap of the vertical electric field component with the optical mode. Since they are very thin, the overlap of quantum dots with the optical mode is very small. Such a small value is hard to calculate accurately. Therefore we calculated the modal electro-optic coefficient, for the entire layer subjected to the electric field. This layer includes both the quantum dots and the bulk GaAs adjacent to quantum dots. In this calculation, we assumed that Γ remained unchanged from a waveguide in which quantum dot layers are replaced by bulk GaAs. This way we obtained an effective electro-optic coefficient which is about 20 % higher than that of bulk GaAs. As a matter of fact, examination of 5.7 reveals that

full on/off modulation is possible using only 6 V. This corresponds to less than 1 V-cm modulation efficiency. In other words, using this modulator as the arms of a push pull driven Mach-Zehnder modulator, less than 1 V drive voltage would result for 1 cm long arms.

In simulations when quantum dot layers are replaced with a bulk GaAs layer on/off modulation voltage is obtained as 7.27 V which indicates more efficient modulation in the quantum dot sample. It should be noted that in this analysis Γ is the only calculated quantity. The observed improvement in the effective electro-optic coefficient could not be due to the difference in Γ between waveguides with GaAs core and waveguides with quantum dot cores. Although index of quantum dot layers is higher than GaAs, they only perturb the waveguide mode slightly due to their very small overlap with the optical mode. The overlap factor of InAs quantum dot layers is calculated using finite difference beam propagation method simulations and is approximately 0.015 for all samples. To get a 20 % improvement in modulation efficiency due to Γ alone would require unrealistically high index for the quantum dot layers. In order to generate a 20 % improvement in the overall modulation efficiency the electro-optic coefficient of the quantum dot layers itself should have improved significantly. Using the QD overlap factor quoted above we estimate that for the QD layer $n^3 r_{41}$ term is about 7-10 times higher than bulk GaAs. This is a very significant improvement. The schematic representation of overlap calculation is given in Figure 5.8

For overlap calculation, first, fundamental mode profile is obtained. Then the proper positions of the quantum dots on this mode profile are determined. The total area and the area corresponding to the quantum dots are integrated and their ratio gives the overlap factor of the quantum dots.

5.4.2 Electro-absorption Measurements

Electro-absorption coefficients were measured using the same set-up given in Figure 5.2. The only difference was operation wavelength. The experiments were conducted at 1300 nm by coupling light from a tunable laser (Santec TSL-320

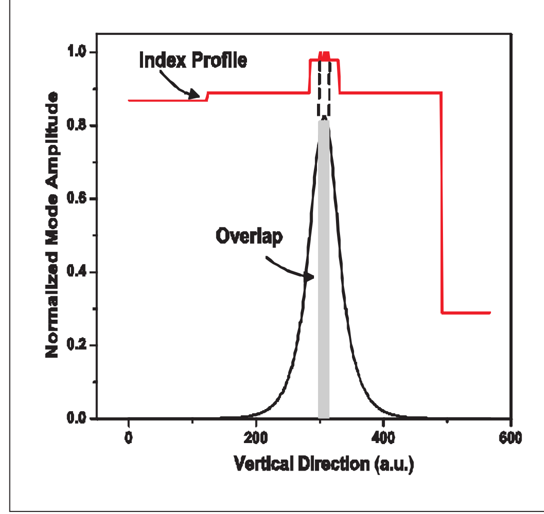

Figure 5.8: The graphical representation of the calculation of overlap factor. The confinement factor is calculated from this overlap region by simply integrating the shaded area.

for 1300 nm) onto one end of the waveguide with a lens shaped fiber. Reverse bias voltage (0-20 V) was applied using a DC voltage source. A wide wavelength range was scanned and at each voltage level, the transmission through the device is recorded as a function of wavelength. The electro-absorption coefficients are obtained using:

$$\alpha_t = 10log\left(r^2 \frac{1+\sqrt[2]{K}}{1-\sqrt[2]{K}}\right) \tag{5.5}$$

where $K = T_{min}/T_{max}$, $r^2 = [(n_e - 1)/(n_e + 1)]^2$ is the facet reflectivity and, n_e is the mode effective index. Since the structure lases at 1285 nm, absorption near 1300 nm is expected. High absorption values at 1309 nm were obtained as expected. Indeed, at 1515 nm, the average insertion loss is 3.1 dB/cm for all samples and at 1309 nm this value increases to 30 dB/cm. Considering that all other factors remain the same, the increase in insertion loss by a factor of 10 is indicative of excitonic absorption. The absorption spectrum of the samples was also studied under applied electric field. Absorption spectra of all samples shift to lower photon energies with increasing electric field. Maximum change of absorption was observed at 1.32 μm as 21% for a reverse bias of 18 Volt for 1 mm

long sample. The absorption curves of 1 mm and 1.6 mm long samples are given in Figure 5.9 and Figure 5.10, respectively.

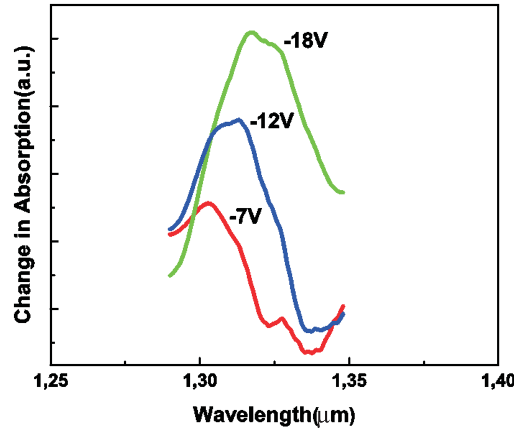

Figure 5.9: Change in absorption due to applied reverse bias for 1 mm long sample. Red shift of the spectra should be noted with increasing applied voltage.

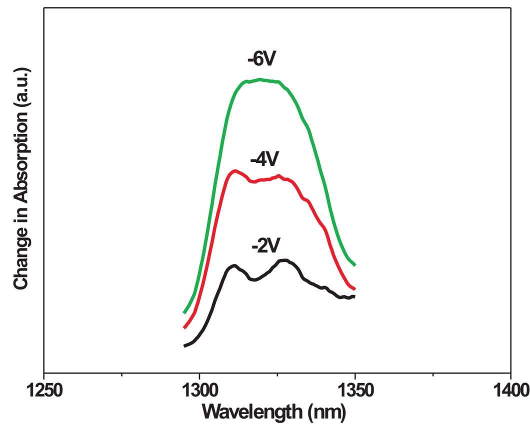

Figure 5.10: Change in absorption due to applied reverse bias for 1.6 mm long sample.

5.5 Conclusions

In conclusion, the low voltage modulation in InAs quantum dot waveguides was observed in this chapter. The electro-optic coefficients of multilayer quantum

dot structures far away from the lasing wavelength were measured at 1500 nm. The linear electro-optic coefficient of InAs QDs is found to be significantly larger than that of GaAs bulk material. The electro-absorption of these multilayer quantum dot waveguides at 1300 nm was also measured. Since these structures were designed as lasers, large absorption near the lasing wavelength (1285nm) was obtained as expected. Absorption edges of the samples shifted to lower photon energies with increasing electric field. Change in absorption spectra as high as 21% was observed at 1.32 μm at 18 Volt bias. These results are promising for QD-based electro-optic and electro-absorption modulators.

Most of the results presented in this chapter have been published in [1].

Chapter 6

Conclusions

When the dimensions of the material are scaled down to nanometer range, the atomic and electronic structures may gain some unique features which make the material favorable for many applications. Si-ncs and Ge-ncs may have a radii close to or smaller than the exciton Bohr radius. Once the diameter becomes smaller than the exciton radius, the energy levels in the particle become quantized and the transitions are locked into specific energy states.

Both Si-nc and Ge-nc are good candidates for flash memory applications. Ge-ncs have smaller band gap compared to silicon. Therefore, Ge-ncs are thought to be better suited for data retention operations than Si-ncs in non volatile memory applications.

One of the major problems involved in nanocrystal research is the inhomogeneity of the particles which causes inhomogeneous broadening effects in the PL and EL spectrum. This problem can be minimized by preparing uniform nanoparticles in the form of quantum wells, wires, or dots. Quantum dot is a zero dimensional structure which is spatially confined in three dimensions and is characterized by a completely discrete energy spectrum. Quantum dots are particularly significant for optical applications due to their theoretically high quantum yield. They are specifically intented for use in quantum computing, laser, light emitting diodes, and photovoltaic devices.

This thesis presents the optical and electrical applications of low dimensional structures. For this purpose silicon and germanium nanocrystals for flash memory applications and InAs quantum dots for optical modulators were studied.

For flash memory applications of nanocrystals, we have studied charge and discharge dynamics of both electrons and holes in PECVD grown and post annealed Ge-nc MOS capacitors. We found that hole retention times are actually shorter than electron retention times for samples annealed at low temperatures. We suggested that the observed reduction of hole retention times is due to interface traps states. However, formation of a Ge rich alloy at the interface with high temperature annealing results in longer retention times, which is promising for actual device operations. These observations emphasize the importance of proper interface engineering for Ge-nc memory devices.

Moreover, the effect of layer thicknesses on charge dynamics of nanocrystal flash memories was studied on Si-nc MOS capacitors. The PECVD gradient growth was applied to different layers. These structures were characterized for charge motions inside the nanocrystal layer and at the oxide-nitride interface.

For modulation applications of quantum dot, InAs/InGaAs quantum dot waveguides were studied. The linear electro-optic coefficients of multilayer quantum dot structures were measured at 1500 nm and it was found that InAs quantum dots have significantly larger electro-optic coefficient than that of GaAs bulk material. The electro-absorption of these multilayer quantum dot waveguides at 1300 nm was also measured. Since these structures were designed as lasers, large absorption near the lasing wavelength (1285nm) was obtained as expected. Absorption edges of the samples shifted to lower photon energies with increasing electric field. Change in absorption spectra as high as 21% was observed at 1.32 μm at 18 Volt bias. These results are promising for QD-based electro-optic and electro-absorption modulators.

Bibliography

[1] I. B. Akca, A. Dana, A. Aydinli, M. Rossetti, L. Li, A. Fiore, and N. Dagli. Electro-optic and electro-absorption characterization of inas quantum dot waveguides. *Opt. Express*, 16(5):3439–3444, 2008.

[2] I. B. Akca, A. Dâna, A. Aydinli, and R. Turan. Comparison of electron and hole charge-discharge dynamics in germanium nanocrystal flash memories. *Applied Physics Letters*, 92(5):052103–052106, Feb. 2008.

[3] D. Amans, S. Callard, A. Gagnaire, J. Joseph, G. Ledoux, and F. Huisken. Ellipsometric study of silicon nanocrystal optical constants. *Journal of Applied Physics*, 93:4173–4179, Apr. 2003.

[4] Y. Arakawa and H. Sakaki. Multidimensional quantum well laser and temperature dependence of its threshold current. *Applied Physics Letters*, 40:939–941, June 1982.

[5] L. Brus. Model for carrier dynamics and photoluminescence quenching in wet and dry porous silicon thin films. *Physical Review B*, 53:4649–4656, Feb. 1996.

[6] C. Busseret, S. Ferraton, L. Montes, and J. Zimmermann. A three charge-states model for silicon nanocrystals nonvolatile memories. *IEEE Transactions on Electron Devices*, 53:14–22, Jan. 2006.

[7] A. Campera, G. Iannaccone, and F. Crupi. Modeling of tunnelling currents in hf-based gate stacks as a function of temperature and extraction of material parameters. *Electron Devices, IEEE Transactions on*, 54(1):83–89, Jan. 2007.

[8] L. T. Canham. Silicon quantum wire array fabrication by electrochemical and chemical dissolution of wafers. *Applied Physics Letters*, 57:1046–1048, Sept. 1990.

[9] D. Chen, Z.-Q. Xie, Q. Wu, Y.-Y. Zhao, and M. Lu. Electroluminescence of si nanocrystal-doped sio_2. *Chinese Physics Letters*, 24:2390–2393, Aug. 2007.

[10] W. K. Choi, V. Ng, S. P. Ng, H. H. Thio, Z. X. Shen, and W. S. Li. Raman characterization of germanium nanocrystals in amorphous silicon oxide films synthesized by rapid thermal annealing. *Journal of Applied Physics*, 86:1398–1403, Aug. 1999.

[11] L. Davis and P. Bhattacharya. Photoluminescence and electro-optic properties of small (2535 nm diameter) quantum boxes. *Appl. Phys. Lett.*, 62(22):12–15, May 1993.

[12] J. S. de Sousa and V. N. Freire. Hole-versus electron-based operations in sige nanocrystal nonvolatile memories. *Applied Physics Letters*, 90(22):223504 – 223507, May 2007.

[13] P. Dimitrakis, E. Kapetanakis, D. Tsoukalas, D. Skarlatos, C. Bonafos, G. B. Asssayag, A. Claverie, M. Perego, M. Fanciulli, V. Soncini, R. Sotgiu, A. Agarwal, M. Ameen, C. Sohl, and P. Normand. Silicon nanocrystal memory devices obtained by ultra-low-energy ion-beam synthesis. *Solid State Electronics*, 48(9):1511–1517, Sep 2004.

[14] P. Fauchet, L. Tsybeskov, C. Peng, S. Duttagupta, J. von Behren, Y. Kostoulas, J. Vandyshev, and K. Hirschman. Light-emitting porous silicon: materials science, properties, and device applications. *Selected Topics in Quantum Electronics, IEEE Journal of*, 1(4):1126–1139, Dec 1995.

[15] L. Ferraioli, M. Wang, G. Pucker, D. Navarro-Urrios, N. Daldosso, C. Kompocholis, and L. Pavesi. Photoluminescence of silicon nanocrystals in silicon oxide. *J. Nanomaterials*, 2007(4):1–5, 2007.

[16] A. Fiore, U. Oesterle, R. Stanley, R. Houdre, F. Lelarge, M. Ilegems, P. Borri, W. Langbein, D. Birkedal, J. Hvam, M. Cantoni, and F. Bobard. Structural and electrooptical characteristics of quantum dots emitting at 1.3 μm on gallium arsenide. *IEEE Journal of Quantum Electronics*, 37:1050–1058, 2001.

[17] A. Gehring and S. Selberherr. Modeling of tunneling current and gate dielectric reliability for nonvolatile memory devices. *Device and Materials Reliability, IEEE Transactions on*, 4(3):306–319, Sept. 2004.

[18] S. Ghosh, A. S. Lenihan, M. V. G. Dutt, O. Qasaimeh, D. G. Steel, and P. Bhattacharya. Nonlinear optical and electro-optic properties of InAs/GaAs self-organized quantum dots. *Journal of Vacuum Science Technology B: Microelectronics and Nanometer Structures, Volume 19, Issue 4, July 2001, pp.1455-1458*, 19:1455–1458, July 2001.

[19] Y. T. Hou, M. F. Li, Y. Jin, and W. H. Lai. Direct tunneling hole currents through ultrathin gate oxides in metal-oxide-semiconductor devices. *Journal of Applied Physics*, 91:258–264, Jan. 2002.

[20] M. Jamei, F. Karbassian, S. Mohajerzadeh, Y. Abdi, M. D. Robertson, and S. Yuill. The preparation of nanocrystalline silicon by plasma-enhanced hydrogenation for the fabrication of light-emitting diodes. *Electron Device Letters, IEEE*, 28(3):207–210, March 2007.

[21] K. Kim, J. Shin, N. Park, C. Huh, T. Kim, K. Cho, J. C. Hong, and G. Y. Sung. Enhancement of light extraction from a silicon quantum dot light-emitting diode containing a rugged surface pattern. *Applied Physics Letters*, 89(19):191120–191123, Nov. 2006.

[22] B. H. Koh, E. W. H. Kan, W. K. Chim, W. K. Choi, D. A. Antoniadis, and E. A. Fitzgerald. Traps in germanium nanocrystal memory and effect on charge retention: Modeling and experimental measurements. *Journal of Applied Physics*, 97(12):124305–124308, June 2005.

[23] C. Lee, T.-H. Hou, and E.-C. Kan. Nonvolatile memory with a metal nanocrystal/nitride heterogeneous floating-gate. *Electron Devices, IEEE Transactions on*, 52(12):2697–2702, Dec. 2005.

[24] S. S. Lee, R. V. Ramaswamy, and V. S. Sundaram. Analysis and design of high-speed high-efficiency GaAs-AlGaAs double-heterostructure waveguide phase modulator. *IEEE Journal of Quantum Electronics*, 27:726–736, Mar. 1991.

[25] L. J. Lembo, F. D. Alvarez, D. Lo, C. A. Tu, P. H. Wisseman, C. Zmudzinski, and J. C. Brock. Optical electroabsorption modulators for wideband, linear, low-insertion-loss photonic links. In A. R. Pirich, editor, *Proc. SPIE Vol. 2481, p. 185-196, Photonic Device Engineering for Dual-Use Applications, Andrew R. Pirich; Ed.*, volume 2481 of *Presented at the Society of Photo-Optical Instrumentation Engineers (SPIE) Conference*, pages 185–196, June 1995.

[26] G. H. Li, K. Ding, Y. Chen, H. X. Han, and Z. P. Wang. Photoluminescence and raman scattering of silicon nanocrystals prepared by silicon ion implantion into sio2 films. *Journal of Applied Physics*, 88(3):1439, 2000.

[27] T. Z. Lu, M. Alexe, R. Scholz, V. Talelaev, and M. Zacharias. Multilevel charge storage in silicon nanocrystal multilayers. *Applied Physics Letters*, 87(20):202110–202113, Nov. 2005.

[28] K. M and B. C. Electronic properties of ge nanocrystals for non volatile memory applications. *Solid-State Electronics*, 50(7):1310–1314, May 2006.

[29] T. C. M. Yang. Charge trapping and retention behaviors of ge nanocrystals distributed in the gate oxide near the gate synthesized by low-energy ion implantation. *Journal of Applied Physics*, 101(12), June 2007.

[30] A. Markus, J. X. Chen, C. Paranthoën, A. Fiore, C. Platz, and O. Gauthier-Lafaye. Simultaneous two-state lasing in quantum-dot lasers. *Applied Physics Letters*, 82:1818–1821, Mar. 2003.

[31] H. S. Mavi, A. K. Shukla, R. Kumar, S. Rath, B. Joshi, and S. S. Islam. Quantum confinement effects in silicon nanocrystals produced by laser-induced etching and cw laser annealing. *Semiconductor Science Technology*, 21:1627–1632, Dec. 2006.

[32] A. Meldrum, A. Hryciw, A. N. MacDonald, C. Blois, K. Marsh, J. Wang, and Q. Li. Photoluminescence in the silicon-oxygen system. volume 24, pages 713–717. AVS, 2006.

[33] D. A. B. Miller, D. S. Chemla, T. C. Damen, A. C. Gossard, W. Wiegmann, T. H. Wood, and C. A. Burrus. Band-edge electroabsorption in quantum well structures: The quantum-confined stark effect. *Phys. Rev. Lett.*, 53(22):2173–2176, Nov 1984.

[34] G. Moreau, A. Martinez, D.-Y. Cong, K. Merghem, A. Miard, A. Lemaître, P. Voisin, A. Ramdane, I. Krestnikov, A. R. Kovsh, M. Fischer, and J. Koeth. Enhanced In(Ga)As/GaAs quantum dot based electro-optic modulation at 1.55 μm. *Applied Physics Letters*, 91(9):091118–091121, Aug. 2007.

[35] Y. Nakamura, K. Watanabe, Y. Fukuzawa, and M. Ichikawa. Observation of the quantum-confinement effect in individual Ge nanocrystals on oxidized Si substrates using scanning tunneling spectroscopy. *Applied Physics Letters*, 87(13):133119–133122, Sept. 2005.

[36] A. Nauen, I. Hapke-Wurst, F. Hohls, U. Zeitler, R. J. Haug, and K. Pierz. Shot noise in self-assembled inas quantum dots. *Phys. Rev. B*, 66(16):161303, Oct 2002.

[37] E. Nicollian. *MOS (Metal Oxide Semiconductor) Physics and Technology*. Wiley-Interscience, 2003.

[38] W. Pan. Photoluminescence from silicon nanocrystals embedded in silicon oxides. *APS Meeting Abstracts*, page 26003, Mar. 2005.

[39] B. Park, S. Choi, H.-R. Lee, K. Cho, and S. Kim. Memory characteristics of mos capacitors with ge nanocrystal-embedded al_2o_3 gate layers. *Solid State Communications*, 143:550–552, Sept. 2007.

[40] C. R. Pollock. *Fundamentals of Optoelectronics.* Richard D Irwin, 2003.

[41] O. Qasaimeh, K. Kamath, P. Bhattacharya, and J. Phillips. Linear and quadratic electro-optic coefficients of self-organized In0.4Ga0.6As/GaAs quantum dots. *Applied Physics Letters*, 72:1275–1278, Mar. 1998.

[42] N. M. Ravindra and J. Zhao. Fowler-nordheim tunneling in thin sio_2 films. *Smart Material Structures*, 1:197–201, Sept. 1992.

[43] S. Schmitt-Rink, D. A. B. Miller, and D. S. Chemla. Theory of the linear and nonlinear optical properties of semiconductor microcrystallites. *Phys. Rev. B*, 35(15):8113–8125, May 1987.

[44] M. She and T.-J. King. Impact of crystal size and tunnel dielectric on semiconductor nanocrystal memory performance. *Electron Devices, IEEE Transactions on*, 50(9):1934–1940, Sept. 2003.

[45] K. Shimomura, S. Arai, and Y. Suematsu. Operational wavelength range of gainas(p)-inp intersectional optical switches using field-induced electrooptic effect in low-dimensional quantum-well structures. *Quantum Electronics, IEEE Journal of*, 28(2):471–478, Feb 1992.

[46] J. Tatebayashi, R. Laghumavarapu, N. Nuntawong, and D. Huffaker. Measurement of electro-optic coefficients of 1.3 self-assembled inas/gaas quantum dots. *Electronics Letters*, 43(7):410–412, 29 2007.

[47] W. C. Tjiu, S. P. Ng, W. K. Choi, V. Ng, and Y. W. Ho. Characterization of ge nanocrystals in co-sputtered ge+sio2 system using raman and tem techniques. In H. B. Harrison, A. T. Wee, and S. Gupta, editors, *Proc. SPIE Vol. 4227, p. 146-156, Advanced Microelectronic Processing Techniques, H. Barry Harrison; Andrew T. Wee; Subhash Gupta; Eds.*, volume 4227 of *Presented at the Society of Photo-Optical Instrumentation Engineers (SPIE) Conference*, pages 146–156, Oct. 2000.

[48] J. Warrender and M. Aziz. Evolution of Metal Nanocrystal Films grown by Pulsed Laser Deposition. *APS Meeting Abstracts*, page 7001, Mar. 2003.

[49] R. Welstand, S. Pappert, C. Sun, J. Zhu, Y. Liu, and P. Yu. Dual-function electroabsorption waveguide modulator/detector for optoelectronic transceiver applications. *Photonics Technology Letters, IEEE*, 8(11):1540–1542, Nov. 1996.

[50] A. R. Wilkinson and R. G. Elliman. The effect of annealing environment on the luminescence of silicon nanocrystals in silica. *Journal of Applied Physics*, 96:4018–4020, Oct. 2004.

[51] B. G. Yacobi. *Semiconductor Materials: An Introduction to Basic Principles.* Springer US, 2003.

[52] Y. Yan, Y. Zhang, G. Meng, and L. Zhang. Synthesis of ZnO nanocrystals with novel hierarchical structures via atmosphere pressure physical vapor deposition method. *Journal of Crystal Growth*, 294:184–190, Sept. 2006.